Chemical Science

PERSPECTIVE

View Article Online
View Journal | View Issue

Nanothermodynamics of metal nanoparticles

Cite this: *Chem. Sci.*, 2014, **5**, 2605

Zhen Hua Li[a] and Donald G. Truhlar*[b]

Received 6th January 2014
Accepted 25th February 2014

DOI: 10.1039/c4sc00052h

www.rsc.org/chemicalscience

Metal nanoparticles have been widely used as functional materials in physics, chemistry, and biology. Understanding their unique thermodynamic properties is essential both for practical applications and from a fundamental point of view. This perspective article is an overview of recent progresses on the nanothermodynamics of metal nanoparticles and it especially highlights as examples our own studies on the structural stability, phases, phase changes, and thermodynamic functions of aluminum nanoparticles. We discuss using statistical sampling by Monte Carlo and molecular dynamics algorithms to calculate nanoparticle properties, nanophase properties, free energies, and nucleation rates, and we tried to understand the results in terms of energy landscapes by using exhaustive enumeration of the multiple structures of Al nanoparticles from all sizes up to $N = 65$ plus selected larger calculations.

Size matters

In 1959, Richard Feynman gave a talk entitled "There's plenty of room at the bottom" at an American Physical Society meeting at Caltech.[1] This talk is often viewed as the source of inspiration for nanoscience. In the talk, Feynman speculated that unusual properties would emerge when the dimensions of the materials approach nanometer size (now usually taken to mean 1–100 nm in diameter (ref. 2) or even 500 nm), and he also speculated on developing nanoscale devices for technology. The invention of the scanning tunneling microscope (STM) brought the promise of nanoscience and nanotechnology into broader consciousness by allowing the scientific community to actually see metal nanoparticles and manipulate them.[3] Now STM and other imaging procedures with nanoscale resolution have become standard techniques in material science and surface science, and the promise of functional nanoparticles is well established.

Metal nanoparticles[4–6] and subnanometer metal clusters have been widely used as functional materials for catalysis, storage, sensing, energy, nonlinear photonics, and medicine. Metal nanoparticles also occur naturally in certain geological environments. They have unique chemical, electronic, optical, and magnetic properties, the understanding of which is a fundamental basic research subject and is essential for the practical applications just mentioned. Two generally accepted sources of the uniqueness of the properties of metal nanoparticles in materials research are the surface effect and quantum size effect.

[a]*Shanghai Key Laboratory of Molecular Catalysis and Innovative Materials, Fudan University, Shanghai 200433, China. E-mail: lizhenhua@fudan.edu.cn*

[b]*Department of Chemistry, Chemical Theory Center, and Supercomputing Institute, University of Minnesota, 207 Pleasant Street Southeast, Minneapolis, MN 55455-0431, USA. E-mail: truhlar@umn.edu*

The surface effect is the increasing ratio of the number of surface atoms to the number of interior atoms as a metal particle becomes smaller. This relationship has an important effect on the physical properties of metal nanoparticles; for example, as will be discussed below, it is a primary reason why the solid–liquid transition temperature of nanoparticles is inversely proportional to particle radius.

The quantum size effect is due to the valence electrons of metal atoms being confined in a small space rather than being delocalized in the conduction band of a bulk solid. If we view the valence electrons as quasi-free, the average spacing between consecutive levels of a metal nanoparticle (sometimes called the Kubo gap[7]) is inversely proportional to the number N of atoms in the nanoparticle. Thus the HOMO–LUMO gap of the metal nanoparticles increases with decreasing particle size.

The above arguments show that the physical and chemical properties of metal nanoparticles are strongly affected by their size, and simple models would imply that they are smooth functions of size. However, when the number of atoms in a nanoparticle is smaller than $\sim 10^2$, adding or removing one atom from the nanoparticle can dramatically change its properties, and experience with small nanoparticles shows that their properties are not a smooth function of number of particles or the radius. As one decreases the size from nm dimensions to Å dimensions, metal particles behave more like molecules or clusters than like particles,[8] but we will continue to use the term nanoparticle if they are larger than 1 nm.

In order to characterize bulk materials, one of the most basic questions we ask is: what are the thermodynamic properties? In this article, we address this question for metal nanoparticles. Based on the above arguments we can see that – unlike macroscopic particles – the thermodynamic properties of metal nanoparticles will depend on particle size, and since we are not in the bulk limit, the conventional thermodynamics of macroscopic metals does not apply.

Nanothermodynamics: the basics

Thermodynamics is a science of very certain consequences, such as conservation of energy. The high degree of certainty follows from the large number of particles in a macroscopic system, because fluctuations of macroscopic variables from their mean values have a magnitude of order $O(N^{-1/2})$, where N is the number of particles. For a bulk metal this is $O(10^{-12})$, but for an Al_{45} nanoparticle it is 15%, and for smaller nanoparticles, it is even larger. Not only do nanoparticles have properties intermediate between clusters and the bulk, and not only do they show large fluctuations, but also nanoparticles have non-uniform properties, even within a given nanoparticle. This is illustrated in Fig. 1, which shows the density as a function of distance from the centre of mass for three nanoparticles.

Nevertheless, by using the appropriate variable, one can still make useful analyses and predictions, but there are dramatic surprises in store if one is only accustomed to bulk thermodynamics.[9,10] For example, not only does the condition of coexistence of phases broaden from a single temperature for a given pressure of a pure material to a range of temperature, but also the very nature of the phase change is different, with the appearance of the slush state.[8,11]

Thermodynamics is conventionally viewed as applying in the limit where all extensive variables tend to infinity, but it can also be viewed as a continuum where atomic-scale structure need not be considered.[12] Inversely, when one is not in the thermodynamic limit, atomic-scale structure is very important. For macroscopic systems, the overwhelming majority of atoms are bulk atoms, and the relative contribution of surface atoms to an extensive quantity is $O(N^{-2/3})$, which is negligible, but for a small nanoparticle most of the atoms are on the surface, and atomic-scale properties such as the lower coordination number of surface atoms are critical.[13]

The fundamental equation for the internal energy U of a single-component material in the absence of an external field is expressed as

$$U = TS - PV + \mu N, \tag{1}$$

where T is the temperature, S is the entropy, P is the pressure, V is the volume, and μ is the chemical potential The Gibbs free energy G, the Helmholtz free energy F, the enthalpy H, and U, S, and V are extensive state functions whereas T, P, and μ are intensive functions which are the first derivatives of one extensive variable with respect to another; for example,

$$\mu = \left(\frac{\partial G}{\partial N}\right)_{T,P} = \left(\frac{\partial U}{\partial N}\right)_{S,V}. \tag{2}$$

For homogeneous macroscopic systems, the chemical potential μ can also be expressed as

$$\hat{\mu} = \frac{G}{N}. \tag{3}$$

However, for nanosystems, due to large fraction of nonbulk atoms, the extensive state functions are no longer linearly proportional to N and thus $\mu \neq \hat{\mu}$. For macroscopic systems, we have the Gibbs–Duhem relation

$$-S\mathrm{d}T + V\mathrm{d}P - N\mathrm{d}\mu = 0, \tag{4}$$

so the three intensive variables (μ, T, P) are not independent. Thus μ is a function of just two independent variables T and P. However, since the extensive state functions of nanoparticles are not linearly proportional to N, μ for nanoparticles is not just a function of T and P, but is also a function of N.

Hill addressed this fundamental difference between macro and nano systems, and he deduced the basic thermodynamic equations for nano-sized materials.[9,10] At first, he called these equations the "thermodynamics of small systems", but later – in 2000 – Chamberlin introduced the term nanothermodynamics as a shortened and more fashionable name for the thermodynamics of small systems.[14] Hill's formulation of nanothermodynamics is based on the ensemble of small systems approach, and in a later development Tsallis proposed another form that is a modified Boltzmann–Gibbs scheme based on the inherent fluctuations in nanosystems.[15] Here we will give a brief introduction to Hill's approach.

For a single-component nanosystem, the equation

$$\mathrm{d}U = T\mathrm{d}S - P\mathrm{d}V + \mu\mathrm{d}N \tag{5}$$

is no longer applicable since it applies to macroscopic systems only. This equation can be generalized by adding another term at the ensemble level rather than at the single-system level. Hill treated an ensemble of $\mathcal{N}$ equivalent and non-interacting nanosystems as a macroscopic system with total energy given by

$$U_t = \mathcal{N}U \tag{5a}$$

total entropy given by

$$S_t = \mathcal{N}S \tag{5b}$$

total volume given by

$$V_t = \mathcal{N}V \tag{5c}$$

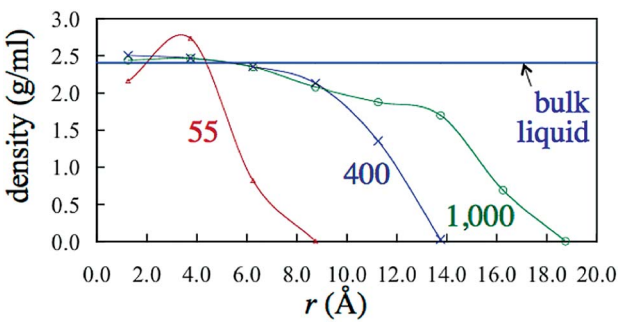

Fig. 1 Nonhomogeneous density distribution in Al_N nanodroplets of three different sizes (N = 55, 400, and 1000) compared to the uniform density of the bulk liquid. All results are for 1000 K.

and total number of particles given by

$$N_t = \mathcal{N}N \tag{5d}$$

etc., where U, S, V, N, *etc.* are considered to be thermodynamic properties of a single small system. Then eqn (5) is augmented to

$$dU_t = TdS_t - PdV_t + \mu dN_t + Xd\mathcal{N} \tag{6}$$

where we have introduced a kind of system chemical potential called the "sub-division potential" and given by

$$X = \left(\frac{dU_t}{d\mathcal{N}}\right)_{S_t,V_t,N_t} \tag{7}$$

Integrating eqn (6) from $\mathcal{N} = 0$ to $\mathcal{N}$ while keeping all small system properties constant the following equation is obtained:

$$U_t = TS_t - PV_t + \mu N_t + X\mathcal{N} \tag{8}$$

Dividing both two sides by $\mathcal{N}$ yields the following equation for a single small system,

$$U = TS - \hat{P}V + \mu N \tag{9}$$

where we have defined $\hat{P} = P - X/V$. By substituting eqn (5a)–(5d), and (9) into (6), we can derive

$$dU = TdS - PdV + \mu dN. \tag{10}$$

Taking differentials in eqn (9) and cancelling the terms in eqn (10), the following relation is obtained:[7]

$$d(\hat{P}V) = -SdT + VdP - Nd\mu \tag{11}$$

This relation is different from that for a macroscopic system since according to eqn (4) the left hand of eqn (11) equals zero for a macroscopic system. Therefore, one fundamental difference between macroscopic systems and nanosystems is that T, P, and μ are all independent for nanosystems. If we choose T, P, and N as the environmental variables, then μ is a function of T, P, and N instead of just T and P for macroscopic systems.

Eqn (9)–(11) are the fundamental equations for nanosystems as a generalization of the thermodynamics of Gibbs for macroscopic systems. The thermodynamics of macroscopic systems can be viewed as a limiting case of nanothermodynamics: For macroscopic systems, U_t is a linear homogeneous function of N_t and thus dX equals zero in eqn (11) according to eqn (7).

The nanothermodynamics of Hill nicely illustrates the differences between macroscopic systems and small systems. However for practical work, further refinements may be useful or even needed; for example Wang and Yang[16] generalized the theory to take into account the size dependence of the surface tension.

Having introduced the basic equations of the nanothermodynamics, we will next focus on the thermodynamics properties of specific metal nanoparticles. Most of the illustrations will be taken from our own work on aluminum nanoparticles[8,17–19] (including a considerable share of previously unpublished material), but for some topics we also give representative (not exhaustive) illustrations or references for other work on metal nanoparticle thermodynamics. We will be concerned entirely with unsupported naked metal clusters, not ligand-stabilized or passivated ones.

The internal energy of a molecule is often taken, to a first approximation, as a sum of potential energy, electronic excitation energy, vibrational energy, rotational energy, and translational energy; the potential energy is a function of internuclear coordinates called the potential energy surface (PES), the set of internuclear coordinates is usually called a geometry, and the geometries where the PES has a local minimum are called structures. The PES is given, according to the Born–Oppenheimer separation of electronic and nuclear motion, as the ground-state electronic energy including, by convention, the nuclear Coulomb repulsion. The validity of the Born–Oppenheimer approximation is that the ground electronic state of the system is well separated in energy from excited electronic states, and this condition is not usually met for metal nanoparticles, just as it is not met for bulk metals. Nevertheless the concept of a potential energy function is almost universally invoked for simulating nuclear motion in such systems despite its known failures.[20] A key advantage of the PES concept is that the ground electronic energy may be approximated by Kohn–Sham density functional theory[21] or wave function theory.[22] For large systems like nanoparticles, affordable yet reliable wave function methods are unavailable, so Kohn–Sham theory is almost always used. The separation into potential energy calculated by Kohn–Sham theory, electronic excitation energy, vibrational energy, rotational energy, and translational energy will be our starting point, although we will eventually modify it to take account of multiple low-energy structures (especially the contribution of configurational entropy to the free energy).

Structures and stability at 0 K

The starting point for the study of any material is to determine its structure, and nanoparticles are no exception to this generalization. We therefore first ask, for nanoparticles of given size N, which structure is the one that is most likely to be prepared and observed in experiments. To answer this question is not easy for two reasons. First, the observed structure may be kinetically controlled.[23] However, our focus here is thermodynamics. Even at equilibrium though, as discussed further below, the stability of a structure at a finite temperature is determined not only by its potential energy but also by its entropy. Despite these caveats, it is often assumed, sometimes incorrectly, that if a particular structure has much lower potential energy than all other possible isomeric structures, this structure will be the one most likely observed in experiments. This minimum-energy structure is called the global minimum (GM) structure, and finding it for various N has been the focus of many research projects in many groups.

To locate GM structures, we need to know the PES and to have an algorithm to locate the global minimum of this multi-dimensional function. For the PES, we have two classes of choices: (i) direct dynamics,[24,25] which means that one solves (approximately, of course) the electronic Schrödinger equation (or equivalent Kohn–Sham equations) for each geometry that occurs in the optimization scheme (or, more generally, in a dynamics calculation) or (ii) using an analytic potential energy function (PEF). For nanoparticles containing dozens or hundreds of atoms, direct dynamics with a reliable approximation scheme for the electronic energies is prohibitively expensive for a full study since a thorough search for all the structures of a metal nanoparticle requires the energies of at least millions of structures to be evaluated. As a consequence, direct dynamics calculations are often carried out with Kohn–Sham theory employing an exchange–correlation functional chosen for low computational cost rather than highest available accuracy (for example, the direct dynamics calculations mentioned below were carried out with the BP86 (ref. 26) and PBE[27] local exchange–correlation functionals rather than with a more accurate hybrid one), and even with a less expensive density functional, the calculations are still too expensive for a full study.

An analytic PEF may be constructed empirically, if enough data is available, but it isn't for metal nanoparticles. A readily available and widely used option has been to use a potential function fitted to bulk data; however, we generated reference data for cohesive energies of aluminum clusters and nanoparticles and found that aluminum PEFs fitted only to bulk data deteriorate seriously in predictive value for $N \lesssim 60$, with the mean unsigned error relative to the reference data typically increasing from <0.2 eV per atom at high N to >0.4 eV per atom at low N.

Although many empirical PEFs have been proposed for nanoparticles, not many have been carefully optimized using accurate structural and energetic data of nanoparticles since accurate experimental data are scarce for nanoparticles.[28] We found that a successful strategy is to fit the PEF to bulk data, nanoparticle data, and cluster data, mainly generated by electronic structure calculations but augmented to the extent possible by any available experimental data, for example, data for metal diatomic molecules and/or data for the bulk metal. For aluminum systems we have recently optimized accurate analytical PEFs[29,30] based on both experimental data and Kohn–Sham calculations employing the hybrid PBE0/MG3 exchange–correlation functional. We note that the PBE0 exchange–correlation functional[31] was chosen to be used on nanoparticles on the basis of extensive validation[32] for aluminum clusters, where benchmark data could be generated. Among them the NP-A and NP-B potentials are the two PEFs with highest accuracy. NP-A includes an accurate two-body potential plus additional terms to account for screening (the interaction between atoms A and B is screened by the presence of atom C) and coordination numbers (other factors being equal, the binding energy per ligand becomes smaller as the number of ligands increases); this is our most accurate potential function but the large number of terms makes it expensive for long simulation on large particles. NP-B has a greatly simplified form that reduces the cost with only a slight decrease in accuracy. The NP-A and NP-B PEFs have accuracies of just 0.03 eV per atom and 0.04 eV per atom, respectively, for aluminum nanoparticles.[30] The results presented for discussion in this perspective are mainly based on the NP-B PEF because it is less expensive to evaluate, which is an important consideration because of the large number of calculations needed to generate thermodynamic data. Although analytic PEFs allow much more exhaustive explorations of structures and thermodynamics than is possible with direct dynamics, one should be aware of their drawbacks, the most important of which is that they do not take cognizance of electronic orbital effects like shell filling and the Jahn–Teller effect.

To illustrate the importance of including nanoparticles in the parameterization, we will revisit the three systems shown in Fig. 1. For the same three systems, Fig. 2 shows the average coordination number as a function of the distance from the centre of mass. For large enough nanoparticles, the coordination number at the surface converges to about 4.5, much lower than the bulk solid (which has a coordination number of 12). The coordination number in the interior converges to 10.5 in good agreement with the experimental value for the liquid, which is 10.6. One must include clusters and nanoparticles in the training set to parametrize reliably for coordination numbers below 10.5.

Having chosen a PEF, the next step is to choose a global optimization method for the location of GM structures.[33,34] Locating GM structures is a difficult task since the energy landscape for a metal nanoparticle is very rugged. For aluminum clusters and nanoparticles, various algorithms have been used to locate the GM structures.[35–40] We adopted a technique that combines the big-bang search method with molecular dynamics (MD) simulation and a quenching method.[17] Once the GM structures are located, we can analyse the structure and stability of the nanoparticles.

For aluminum particles, Al_{19} has a diameter of approximately 1 nm. Thus Al_N particles with $N \geq 19$ are tentatively called nanoparticles while those with $N < 19$ are called clusters. However, one must bear in mind that there is no clear boundary between clusters and nanoparticles. Nevertheless it is interesting to point out that both experimental[41] and computational[42,43]

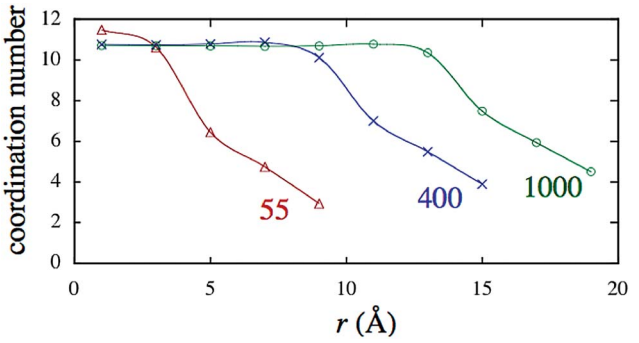

Fig. 2 Coordination numbers in Al_N nanodroplets of three different sizes (N = 55, 400, and 1000). All results are for 1000 K.

evidence for Mg clusters indicates that metallic bonding set in at N equal to about 18–20, although the nonmetal to metal transition is gradual and not precisely defined. As one goes to even larger N, the size of the nanoparticles grows only slowly with N. For example, the longest internuclear distance in the GM structure of Al_{65} is 1.33 nm. If each Al atom is surrounded by a van der Waals sphere (with a van der Waals radius[44] of 0.184 nm), the diameter of this nanoparticle is 1.70 nm. A similar calculation on Al_2 (internuclear distance 0.27 nm) would give a subnanometer size of 0.64 nm.

As is well known, the low-energy structures of small nanoparticles differ from bulk structures. The bulk structure of Al is face-centred cubic (FCC), which is a close packed structure in which each Al atom has a coordination number of 12. For small N though, icosahedral structures are favoured, as illustrated in Fig. 3. In the vicinity of $N = 55$, the FCC structures begin to become competitive with the icosahedral ones. For $N \gtrsim 130$, FCC becomes consistently favored over hexagonal close packed.

The cohesive energy of the GM structure of a nanoparticle is defined by

$$\mathrm{CE}(N) = E_e(1) - E_e^{(1)}(N)/N, \quad (12)$$

where $E_e(1)$ is the potential energy of a single atom and $E_e^{(\gamma)}(N)$ is the potential energy of the classical-equilibrium structure of the isomer γ of the particle of size N (γ is not needed for $N \leq 2$), and we have set $\gamma = 1$ on the right hand side of eqn (12) to denote the GM structure. Cohesive energy can be used in various ways to characterize the stability of a nanoparticle. Excess energy $\Delta(N)$ is one that is defined as

$$\Delta(N) = N^{1/3}[\mathrm{CE}(N) - E_{coh}], \quad (13)$$

where E_{coh} is the cohesive energy of the bulk. Another quantity that can be used to characterize the stability is the second finite energy difference $\Delta_2 E_e^{(1)}(N)$ which is defined as

$$\Delta_2 E_e^{(\gamma)}(N) = E_e^{(\gamma)}(N-1) + E_e^{(\gamma)}(N+1) - 2E_e^{(\gamma)}(N), \quad (14)$$

Results for $\Delta_2 E_e^{(1)}(N)$ ($N = 19$–139) and $\Delta(N)$ ($N = 19$–310) for the aluminum nanoparticles are presented Fig. 4 and 5,

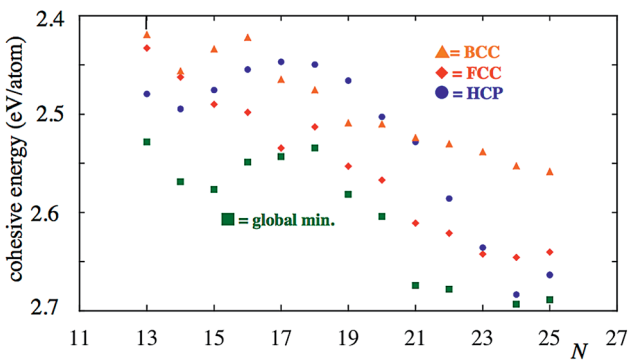

Fig. 3 Cohesive energies of Al_N nanoparticles for the global minima and for three bulk crystal habits (FCC, hexagonal close-packed, and body-centered cubic). Structure classification is based on the parameter of Honeycutt and Andersen.[48] All results are for 0 K.

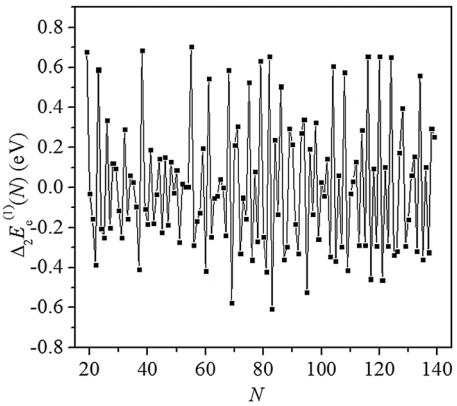

Fig. 4 Second finite energy difference ($\Delta_2 E_e^{(1)}(N)$, in eV) of aluminum nanoparticles. Plotted using data from ref. 17 and 38.

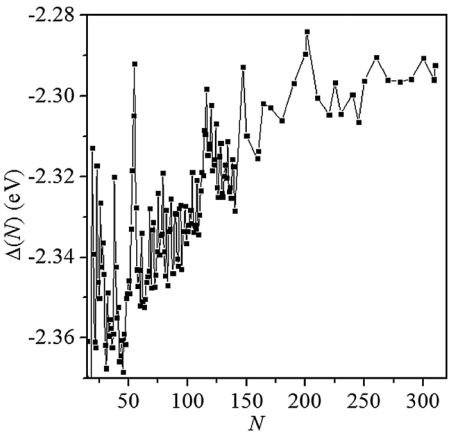

Fig. 5 Excess energy ($\Delta(N)$, in eV) of aluminum nanoparticles. Plotted using data from ref. 17 and 38.

respectively.[17,38] The peaks in the plots correspond to nanoparticles with higher stability than their neighbours. The sizes of the nanoparticles with extremely high stability are called magic numbers. Based on both $\Delta_2 E_e^{(1)}(N)$ and $\Delta(N)$, we can see that 19, 23, 38, 55, 79, 116, 147, and 201 are the magic numbers of the aluminum nanoparticles. Fig. 6 shows the magic-number structures and shows that they are all highly symmetrical structures. The GM structure of Al_{19} is a double icosahedron structure with two interior atoms. The GM structure of Al_{23} can be viewed as a triple icosahedron with three interior atoms. The GM structures of Al_{38}, Al_{79}, and Al_{116} are all truncated octahedra that can be cut out of face-centred-cubic (FCC) bulk. The GM structures of Al_{55} and Al_{147} are icosahedra with Al_{55} having an icosahedron core of 13 atoms while Al_{147} has an icosahedron core of 55 atoms. For the aluminum nanoparticles larger than Al_{300}, Shao and Wu *et al.* found that the majority of the GMs are truncated octahedra.[39,40]

The existence of magic numbers is a common property of metal nanoparticles. Similar phenomena have been observed for, among others, sodium and gold particles[45] and even fictitious particles held together by Lennard-Jones potentials.[46] Two models have been proposed to understand this. The first one is

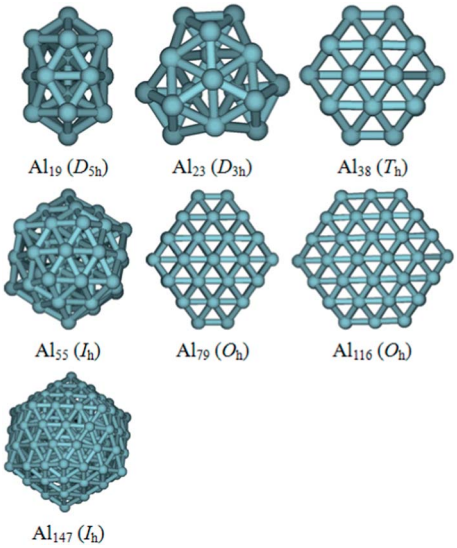

Fig. 6 GM structures of Al_{19}, Al_{23}, Al_{38}, Al_{55}, Al_{79}, Al_{116}, and Al_{147}. Cartesian coordinates taken from ref. 17 and 38 are used to draw the structures.

the geometrical model, which is based on shells of atoms.[47] As mentioned above, the fraction of surface atoms is high in a nanoparticle. As a result the surface tension of nanoparticles is high. In order to reduce surface tension, nanoparticles tend to adopt a more compact and spherical structure. Therefore, nanoparticles with more compact and spherical geometry will have higher stability than other nanoparticles.

The second model for understanding the stability of metal particles is the electronic model, which is based on shells of electrons.[50] The simplest electronic shell model is the jellium model. In this model, the valence electrons of the metal atoms are viewed as particles in a box, and the nuclei are treated as a uniform positively charged background. Thus the densities of states and the energies of the electrons depend crucially on the size of the box. When atoms are added and the shells of the electrons are filled up, the dependence of nanoparticle properties on size is thus no longer smooth, and the largest changes in energy occur when a new shell at higher energy starts to be populated. Nanoparticles with filled electron shells have extra stability. Fig. 7 is an example of the electrons filling the energy levels of a spherical Na_{40} particle in the jellium model.

We can compare these models for their relevance to the aluminum clusters. Consider first the geometrical model. There are several methods to build nearly spherical nanoparticles. The first one is to cut from bulk crystal structure. The spherical nanoparticles cut in this way from FCC bulk are truncated octahedra whose size is expressed by

$$N_{\mathrm{TO}}(n_{\mathrm{l}},\ n_{\mathrm{cut}}) = \frac{1}{3}\left(2{n_{\mathrm{l}}}^3 + n_{\mathrm{l}}\right) - 2{n_{\mathrm{cut}}}^3 - 3{n_{\mathrm{cut}}}^2 - n_{\mathrm{cut}}, \qquad (15)$$

where n_{l} is the length of the edges of the complete octahedron, and n_{cut} is the number of layers cut at each vertex. Therefore, with n_{cut} equal to 1 or 2, the sizes of perfect truncated octahedra are 13, 14, 38, 55, 79, 116, 140, 201, 225, …

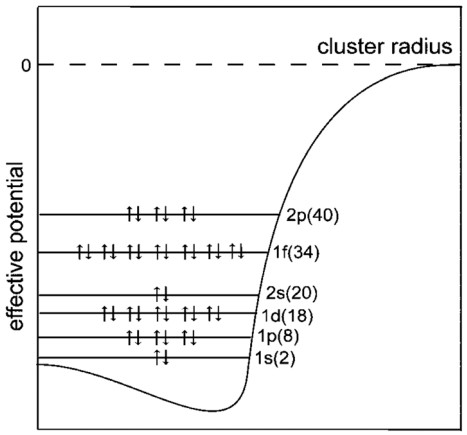

Fig. 7 Electron shells in the jellium model for the 40 valence electrons of the Na_{40} particle. Reprinted from ref. 49 with permission from ACS publications.

The second method is to build Mackay icosahedra whose size is expressed by

$$N_{\mathrm{Ih}}(k) = \frac{10}{3}k^3 + 5k^2 + \frac{11}{3}k + 1, \qquad (16)$$

where k is the number of the shells of the icosahedron. Thus the sizes of perfect icosahedra are 13, 55, 147, 309, …

The third method is to build truncated decahedra. The expression for the size of a Marks decahedron is

$$N_{\text{M-Dh}}(k) = \frac{10}{3}k^3 + 10k^2 + \frac{11}{3}k + 1, \qquad (17)$$

which produces the sequence of 18, 75, 192, …

Finding that Al_{19} and Al_{23} have a building block of Al_{13} icosahedra, that Al_{55} and Al_{147} are icosahedra, and that Al_{38}, Al_{79}, Al_{116}, and Al_{201} are truncated octahedra indicates that the criterion based on surface effects is an important factor in the stability of aluminum nanoparticles. However, this conclusion is based on the approximate PEFs that may overestimate the stability of more symmetrical structures. Direct dynamics calculations show that the GM of Al_{19} has a C_1 symmetry and the double icosahedral structure is high in energy.[51,52] For larger Al_{55} and Al_{147} nanoparticles, density functional calculations with the BP86 exchange–correlation functional indicate that the truncated decahedral structure of Al_{55} and truncated octahedral structure of Al_{147} are more stable than their corresponding icosahedral structures.[52] Although these results differ from those obtained with NP-B, they still indicate that geometrically determined surface effects control the stability of larger aluminum nanoparticles.

Next consider the electronic shell model. Assuming that metal particles are spherical, the jellium model predicts that the magic numbers for sodium clusters are 2, 8, 20, 40, 58, 92, 139, … This is in very good agreement with experiment.[53] For aluminum nanoparticles, each aluminum atom has three valence electrons and thus the candidates for magic aluminum particles are Al_{13}^-, Al_{19}^-, Al_{31}^-, Al_{46}^-, *etc.* Al_{13}^- has been verified by experiment to be a very stable cluster, which is rationalized by a double complete shell structure, that is, an

icosahedron with a complete atomic shell and a complete electronic shell.[54] For its superior stability and its properties resembling those of halogen anions, it is often called a superatom,[55,56] as is the neutral cluster with $N = 13$. The latter, being one electron shy of a closed shell is found to have strong resemblance in its reactivity trends to a halogen atom.

For Al_N^+ with $N = 25$–83, the Jarrold group[57] found a strong correlation between the cohesive energies at temperatures below the melting temperature and the latent heat for melting. They found evidence of an electronic shell closing at $N = 37$ and a structural shell closing at $N = 44$. One should keep in mind that the optimum structures are not the same for neutral nanoparticle and the cation.

Wu and coworkers[38] used the NP-B potential to optimize the GM structure for $N = 38$, 63–140, and 27 values of N in the range 147 to 310. In two follow-up papers,[39,40] again employing the NP-B potential, they found the GM structure for 55 additional values of N, this time in the range 314 to 800. They found that the structures in the size range 270–405 correspond to adding surface atoms to truncated octahedra until a 405-atom truncated octahedron is built up, then adding surface atoms to that structure until reaching a truncated octahedron with 586 atoms, then adding surface atoms to that until reaching a 711-atom truncated octahedron. They also found patterns in whether the surface atoms add to (100) or (111) faces. Finally they compared the energies of all truncated octahedra up to 9879 atoms, which were classified into 13 families.

In general the electronic shell model seems most useful for low N and the geometrical shell model becomes more useful at large N. Although the stability of all metal nanoparticles is surely affected by electronic orbital energies, the electronic shell model seems to be less useful for aluminum clusters than for sodium clusters. For sodium clusters, electronic shell effects appear to be important even for $N > 1000$.[5,58] Aluminum particles have a much higher cohesive energy than sodium particles, which results in less flexible structures for aluminum particles than for sodium particles. Therefore, aluminum particles are less spherical than sodium particles. Independent of the validity of the spherical jellium model for determining the most stable structures, it has less applicability to understanding the ensemble of structures nanoparticles with each N, which we consider next.

Structures and stability at finite temperatures

The number of possible isomeric structures of a nanoparticle of size N is very large. In the past, researchers have often focused on the properties of the GM structure, although in some studies[59,60] a few low-lying isomers for a given N were identified. To some extent, focusing only on the lowest-energy structure or structures for each N is useful to understand the structural evolution of nanoparticles because, all other things being equal, lower-energy structures have greater equilibrium populations due to larger Boltzmann factors. Thus the population of the GM structure, due to its low energy, is often high, and in such cases its properties can be used to represent the behaviour expected for the nanoparticle. However this is not always true since the population P_γ of an isomer structure γ is not solely determined by its potential energy. Instead we have:[17]

$$P_\gamma = \frac{e^{-E_e^{(\gamma)}/k_B T} q_{Rov}^{(\gamma)} q_{Elec}^{(\gamma)}}{\sum_\gamma e^{-E_e^{(\gamma)}/k_B T} q_{Rov}^{(\gamma)} q_{Elec}^{(\gamma)}}, \quad (18)$$

where $E_e^{(\gamma)}$ is the potential energy of the isomer γ relative to the GM structure, $q_{Rov}^{(\gamma)}$ is the rovibrational partition function of the isomer γ, k_B is the Boltzmann constant, and $q_{Elec}^{(\gamma)}$ is the electronic partition function, which in the present part of the discussion will be assumed to be a constant so it cancels out. Although the GM structure has the lowest energy, its rovibrational partition function $q_{Rov}^{(1)}$ is often smaller than that of the other structures, especially when it is a well ordered structure, since such structures tend to be smaller (more compact than higher-energy isomers) with higher vibrational frequencies and higher symmetry numbers, both of which decrease the partition function. For example, the vibrational frequency distribution of the Al_{61} nanoparticle (Fig. 8) indicates the third lowest-energy isomer has more soft vibrational modes than the GM structure. In our work, we searched for all structures for each N, and we included all found structures in our calculations of partition functions.

Adopting the approximate rigid-rotor and harmonic-oscillator (RRHO) approximation for $q_{Rov}^{(\gamma)}$, the population of each isomer for a given nanoparticle can be computed according to eqn (18). The results are shown in Fig. 9 for Al_{19} and Al_{61}. Fig. 9 shows that the population of the GM of Al_{19} drops gradually beyond 700 K. In sharp contrast the population of the GM of Al_{61} is already close to zero at room temperature while the population of the third isomer is higher than 90% at room temperature. During MD simulations we can quench intermediate structures. The population of an isomer structure among all the quenched structures can thus be obtained from the simulations.[8] The populations of the GM structures (P_1) of Al_{19}, Al_{37}, Al_{38}, and Al_{61} are plotted in Fig. 10. The P_1 plots show that P_1 of Al_{61} drops to zero beyond 500 K, which is different from the results computed from partition-function calculations employing the RRHO approximation. On the other hand, P_1 of

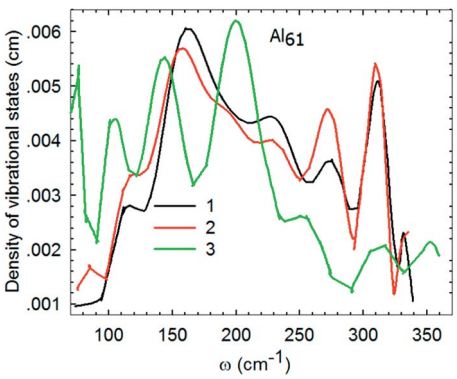

Fig. 8 Density of vibrational states of the three lowest-energy isomers of Al_{61} with "1" representing the global minimum, "2" the second lowest-energy isomer, and "3" the third lowest-energy isomer. Reprinted from ref. 17 with permission from ACS publications.

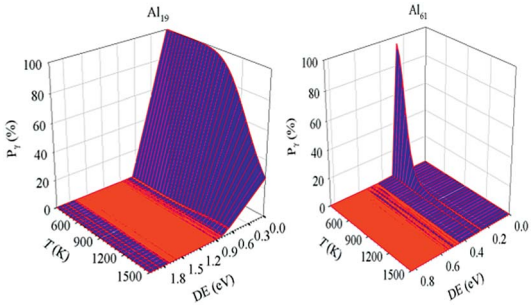

Fig. 9 Three-dimensional representation of P_γ (defined by eqn (18)) *vs.* T and relative energy ΔE (labeled DE in the plot) for $N = 19$ (left) and 61 (right). Adapted from ref. 17 with permission from ACS publications.

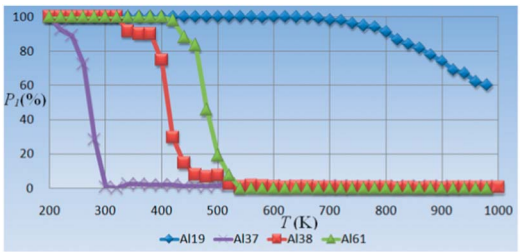

Fig. 10 Population of the GM structure from MD simulations.

Al_{19} drops beyond 700 K, in accordance with the results from partition-function calculations. Nevertheless, the qualitative trends obtained from both the partition-function calculations and the MD simulations are the same: P_1 drops to zero with population diverted to higher-energy isomer structures as temperature is elevated.

In order to understand the above trends better, it is useful to make a more detailed comparison of Al_{37} and Al_{38}. The twelve lowest-energy structures of Al_{37} are shown in Fig. 11, and the

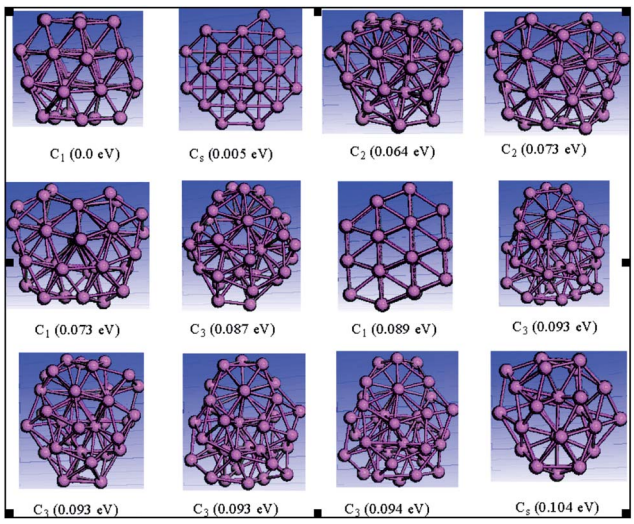

Fig. 11 Lowest-energy structures of Al_{37} and their symmetry and isomeric excitation energy.

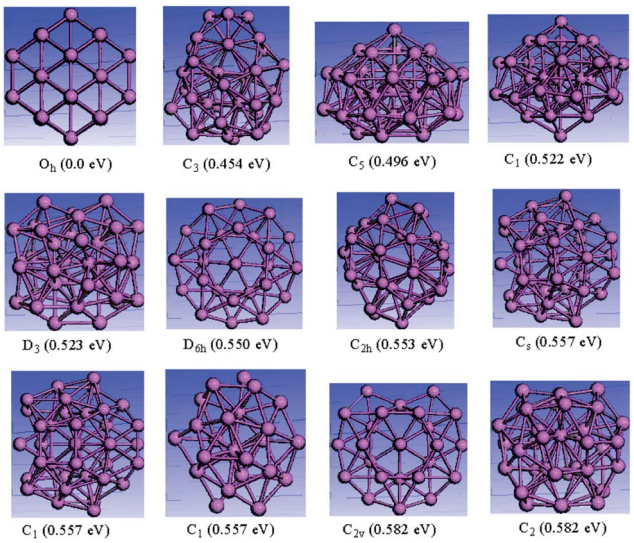

Fig. 12 Lowest-energy structures of Al_{38} and their symmetry and isomeric excitation energy.

twelve lowest of Al_{38} are shown in Fig. 12. We see that Al_{37} has many low-energy structures, and Al_{38} is a truncated octahedron with a gap of 0.45 eV between the energies of the two lowest isomers. At 300 K, the lowest-energy structure of Al_{37} has a population less than 0.2%, and the four lowest states have a population of only 20%, whereas for Al_{38} the four lowest structures have a population of 99%. At 1500 K, the lowest 64 states have a population 17% for Al_{37} and a population of 15% for Al_{38}.

The above analysis raises two crucial questions: (1) Since P_1 becomes zero at high temperature, can the properties of a nanoparticle be represented by the properties of its GM structure? (2) Are the magic nanoparticles still magic at elevated temperatures?

To answer the first question, one can define a parameter to characterize the difference between the properties of the nanoparticle and its GM structure. For this purpose, the following particle isomeric energy is defined, which is the energy difference (including thermal contributions) between the GM structure and the nanoparticle:

$$E_{\mathrm{Iso}} = \sum_{\gamma}\left(\nu E_{\mathrm{e}}^{(\gamma)} + E_{\mathrm{Vib}}^{(\gamma)} + E_{\mathrm{Rot}}^{(\gamma)} - E_{\mathrm{Vib}}^{(1)} - E_{\mathrm{Rot}}^{(1)}\right)P_\gamma$$
$$= -\left(E_{\mathrm{Vib}}^{(1)} + E_{\mathrm{Rot}}^{(1)}\right) + \sum_{\gamma}\left(\nu E_{\mathrm{e}}^{(\gamma)} + E_{\mathrm{Vib}}^{(\gamma)} + E_{\mathrm{Rot}}^{(\gamma)}\right)P_\gamma, \qquad (19)$$

where $E_{\mathrm{Vib}}^{(\gamma)}$ and $E_{\mathrm{Rot}}^{(\gamma)}$ are the vibrational and rotational contributions, respectively, to the thermal energy of isomer γ.

From the E_{Iso} plots presented in Fig. 13, it can be concluded even 300 K is a high enough temperature that many nanoparticles cannot be represented by their corresponding GM structures. At 800 K, only Al_{19} and Al_{56} can be represented by their corresponding GM structures. At 1500 K, no nanoparticles can be represented by their corresponding GM structures. The magic nanoparticle Al_{19} is well represented by its GM structure in a wide temperature range up to 800 K, while Al_{23} is well

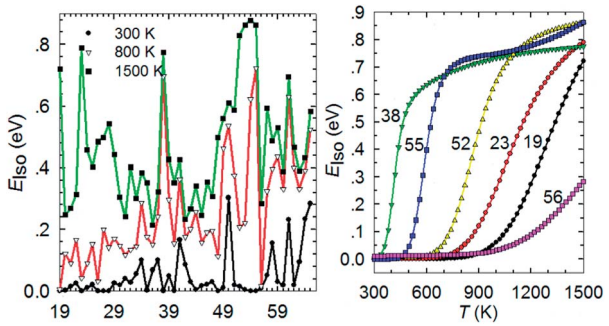

Fig. 13 Isomeric energy (eV) as a function of size (left) and temperature (right) for the aluminum nanoparticles.

represented up to 700 K, Al_{55} up to 450 K, and Al_{38} only up to 350 K. We conclude that the properties of the nanoparticles cannot be represented by the properties of the GM structure or any other single isomer structure in a wide temperature range. Surprisingly, the properties of some of the non-magic nanoparticles, *e.g.* Al_{52}, and Al_{56} (Fig. 13, right panel) can be well represented by the properties of their corresponding GM structures in a wider range of temperatures than the magic ones, Al_{38} and Al_{55}.

The case of Al_{56} is particularly interesting.[17] We found that there are 53 isomers with energies within 0.02 eV of the lowest-energy one. The GM and the next two lowest-energy isomers are obtained by adsorbing an Al atom onto the icosahedral Al_{55} global minimum. The other 50 isomers can be obtained by inserting one aluminum atom into a five-member ring formed by surface aluminum atoms of the icosahedral Al_{55} global minimum to make a six-membered ring. As a result, these 53 isomers have very similar structures to the global minimum so that, although many structures contribute to thermodynamic averages, the properties of the global minimum may still be representative.

Kang and coworkers[61] studied the cases of $N = 51$–58 and 64 by direct dynamics. The analysis was complicated because the dynamically calculated structures were sometimes trapped in metastable states over the limited time frame examined. (In comparison the method we used corresponds by construction to an equilibrated ensemble. Kinetic complications in studying the melting experimentally have been discussed by Jarrold *et al.*[62]) Their interpretation leaned heavily on the symmetry of the GM structure. For $N = 55$ they found structures exhibiting diffusion of surface atoms around a rigid core that they labelled as half-solid; these structures resemble the structures discussed above for $N = 56$.

These observations indicate that when studying metal nanoparticles using theoretical means, it is sometimes informative to study just the properties of a single structure, but in other cases it is useless, even when considering the GM structure or even the GM structure of a magic nanoparticle. Gong and coworkers in a MD simulation study of water clusters reached similar conclusions.[63] This multi-structural situation indeed presents a challenge to theoretical studies of metal nanoparticles. Recently, in a direct dynamics MD simulation on the supported Pt_nSn_m nanoparticles at the catalytically relevant temperature of 598 K, Vila *et al.* show that the particles exhibit large fluctuations in morphology.[64] By studying the adsorption of H_2 on the Pt_nSn_m nanoparticles they concluded that it is important to think about a catalyst as a dynamically fluctuating object rather than a static one.

We have limited results for the ease or difficulty of passage among the multiple low-energy structures in the Al nanoparticles. In a study of Al_{61} we found transitions from the lowest-energy structure to the second-lowest energy structure and to higher-energy structures on the ns time scale at 450 K. Studying the barriers between stable states would be an interesting project for future work. These simulations did not include electronically nonadiabatic transitions, but in general one expects surface crossings between low-energy electronically excited states (the barriers connecting minima on a potential energy surface are usually located on shoulders of conical intersections[65]). Mapping out the topography of such surface crossings and the associated dynamical behaviour is another interesting subject for future work.

To answer the second question, we define a quantity similar to $\Delta_2 E_e^{(1)}(N)$, in particular the second finite Gibbs free energy difference:

$$\Delta_2 G_T(N) = G_T^{(t)}(N-1) + G_T^{(t)}(N+1) - 2G_T^{(t)}(N), \qquad (20)$$

where $G_T^{(t)}(N)$ is the Gibbs free energy of the nanoparticle, all the low-energy isomer structures quenched from the MD simulations, with size N at T. Fig. 14 shows that at 300 K, the $\Delta_2 G_T(N)$ *vs.* N plot still show peaks at $N = 19$, 23, 38, and 55. However, at 1500 K, these peaks either disappear or even become valleys. For example, for $N = 19$ and 38, the peaks become valleys at 1500 K, indicating Al_{19} and Al_{38} nanoparticles become less stable than their neighbouring nanoparticles. In addition, new peaks arise at 1500 K and some valleys at 300 K turn into peaks at 1500 K. For example, new peaks at $N = 20$ and 36 emerges while the valleys at $N = 22$ and 39 turn into peaks. Therefore, magic nanoparticles at low temperatures become non-magic, while non-magic ones become magic at elevated temperatures. The relative stability of nanoparticles is thus temperature dependent. The entropy contribution must be considered not only at elevated

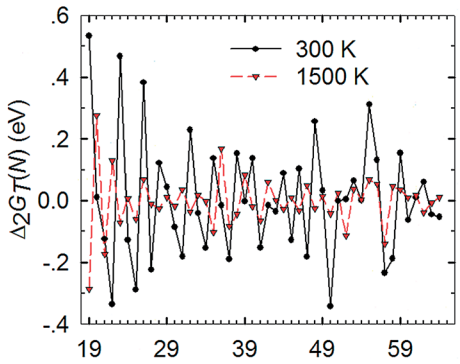

Fig. 14 Second finite Gibbs free energy difference ($\Delta_2 G_T(N)$, in eV) of aluminum nanoparticles.

temperatures, for example, to understand melting (considered in the next section) but also at room temperature.

Nanophases: solid, slush, and liquid phases

Cleveland *et al.*[66] studied the melting of gold nanoclusters with $N = 75$, 146, and 459 and pointed out the importance of solid-to-solid transitions in the melting region. This has become a theme, although various interpretations[67–73] differ in detail, sometimes emphasizing surface melting or a so-called soft solid or fluxional cluster. These references are just a small fraction of the available work on nanoparticle melting because, unlike some of the other topics discussed in this perspective, the question of melting of nanoparticles has been extensively studied. In the space available, we will not attempt an exhaustive coverage of the literature but rather will focus on a selected subset of this work that brings out concepts we think should be emphasized, and we especially discuss our own melting simulations which have the advantage that one can relate the results to our extensive studies of the potential energy landscape and which may also be of interest because our analysis is built on a different point of view than most of the previous work.

For macroscopic systems, a phase is well defined and it corresponds to a region of space throughout which all physical properties of a material, such as density, chemical composition, and index of refraction are essentially uniform or continuously varying.[74] Solid, liquid, gas, and plasma phases are the four phases of matter. The transition from one phase to the other is either a first-order or a second-order phase transition. The first-order phase transition involves a latent heat and is often accompanied by an abrupt change in some physical properties. A small change in temperature or pressure is able to change the phase completely from one to another. Thus, the change of phase can be characterized by a transition temperature T_t. Melting and evaporation of macroscopic systems are prototype first-order phase transitions. However, the phases of nanosystems are not well defined. Do nanoparticles have phases similar to those in macroscopic systems, for example solid and liquid phases? How can one determine the phases of nanoparticles? Do they have phase transitions similar to those in macroscopic systems? To answer these questions, extensive molecular dynamics simulations have been performed on the melting transitions of aluminium nanoparticles.[8]

Starting from 200 K, a nanoparticle with its GM structure was gradually heated to high temperatures, and then various physical properties of the nanoparticle were computed. From the evolution of these physical properties with temperature, information about the phases and phase transition of nanoparticles was extracted. Heat capacity, which is the derivative of the caloric curve with respect to temperature, is one physical property widely used to characterize melting transition for both macroscopic systems and nanosystems. For some systems the heat capacity has a sharp peak at a transition temperature, while for others the heat capacity has no sharp peak. The former kind of system has a first-order transition, while the latter has a second-order transition. However, one must be cautious with the use of heat capacity to characterize melting transitions because we have shown that a peak in the heat capacity curve is not necessarily related to a phase transition.[8] It may just correspond to a change from high population of one isomer to high population of another, or to a transition from one electronic state to another. The heat capacity of a system with two states in equilibrium with each other can be shown to be:

$$C = \frac{\Delta\varepsilon^2/k_B T^2}{\left(e^{\Delta\varepsilon/2k_B T} + e^{-\Delta\varepsilon/2k_B T}\right)^2}, \quad (21)$$

where $\Delta\varepsilon$ is the energy separation between the two states. From Fig. 15 it can be seen for this model system the heat capacity curve as a function of temperature has a peak. The sharpness of the heat capacity curve is determined by the energy separation between the two states. The narrower the separation the sharper is the peak and the lower is the temperature of the peak position. Therefore, one should use more than just the heat capacity to characterize a melting transition; because the phase change is a subtle issue, one should gather as much information as possible.

The Lindemann parameter is another quantity that is widely used to characterize melting transitions for bulk materials.[75] The Berry parameter[76] is an extension of the Lindemann parameter, and it is the relative root-mean-square fluctuation in the interatomic separation:

$$\Delta_B = \frac{2}{N(N-1)} \sum_{i<j} \frac{\sqrt{\langle r_{ij}^2 \rangle - \langle r_{ij} \rangle^2}}{\langle r_{ij} \rangle}, \quad (22)$$

where r_{ij} is the interatomic distance between atoms i and j. This parameter is widely used in simulations of clusters and nanoparticles. For a solid state, the Berry parameter is usually below 0.10, while for a liquid state, it is usually above 0.30. In both kinds of states the Berry parameter increases linearly but slowly with temperature. Near the temperature of transition, the parameter has an abrupt jump. In our simulations, we found that the Berry parameter converges slowly, and very long simulation times are needed to get converged results; hence it is not as useful as we had anticipated.

Other properties we explored include: (1) the average distance of atoms to the centre of mass (CoM), as given by

$$R_{CoM} = \frac{1}{N} \sum_i |\mathbf{r}_i - \mathbf{r}_{CoM}|, \quad (23)$$

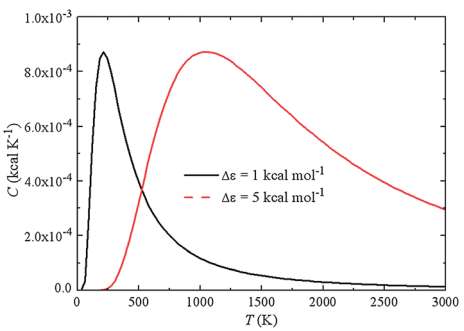

Fig. 15 Heat capacity curve of a two-state system. Reprinted from ref. 8 with permission from ACS publications.

where $\mathbf{r}_i$ and $\mathbf{r}_{CoM}$ are the positions of atom i and the CoM, respectively. (2) Radius of gyration:

$$R_g = \sqrt{\frac{1}{N}\sum_i |\mathbf{r}_i - \mathbf{r}_{CoM}|^2}. \quad (24)$$

(3) Volume:

$$V = \frac{4}{3}\pi R_1 R_2 R_3, \quad (25)$$

where R_i (i = 1, 2, 3) are the three radii of a non-spherical nanoparticle which are related to the principal moment of inertia I by:

$$R_i = \sqrt{5/2}\sqrt{I_i/M}\ (i = 1, 2, 3), \quad (26)$$

where M is total mass of the nanoparticle. (4) Coefficient of thermal expansion:

$$\beta = \frac{1}{V}\frac{dV}{dT}. \quad (27)$$

(5) Isothermal compressibility:

$$\kappa = \frac{1}{k_B T}\frac{1}{V}\frac{\langle V^2\rangle - \langle V\rangle^2}{\langle V\rangle}. \quad (28)$$

Other workers have also used the projected density of vibrational states of the instantaneous normal modes of an MD simulation.[77]

In Fig. 16 the heat capacity *vs.* temperature curves are presented for selected aluminum nanoparticles; the ordinate is the dimensionless $C/N_f k_B$ with N_f being the number of degrees of freedom of the nanoparticle ($N_f = 3N - 3$). The left part of Fig. 16 shows some nanoparticles that have sharp peaks in the heat capacity curve, while the right part presents some without a sharp peak. The natural logarithm of κ and the relative volume (relative to that at 200 K) of the same aluminum nanoparticles as shown in Fig. 16 are presented in Fig. 17 and 18, respectively.

Fig. 16 shows that those particles with sharp peaks in the heat capacity *vs.* T curve have heat capacities that increase approximately linearly before the peak and decrease approximately linearly after the peak. In addition, the peak becomes sharper with the increase of nanoparticle size indicating a narrower temperature window for the change. It should be noted that the position of such a peak does not simply move from lower temperature to higher temperature as size increases;

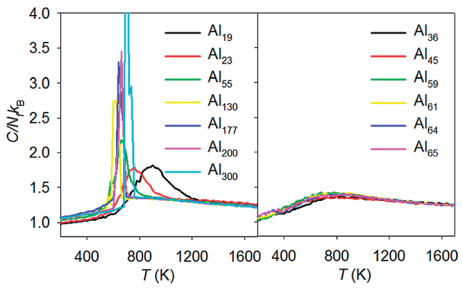

Fig. 16 Heat capacity *vs.* T curves of aluminum nanoparticles. Left: with sharp peaks; right: no sharp peaks.

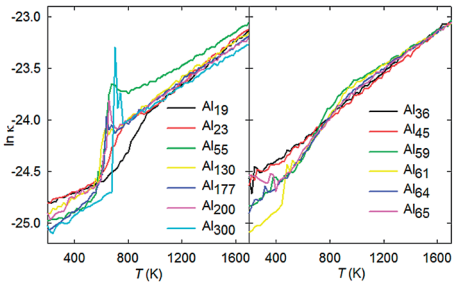

Fig. 17 ln κ *vs.* T curves of aluminum nanoparticles. Results are shown for the same nanoparticles as in Fig. 16.

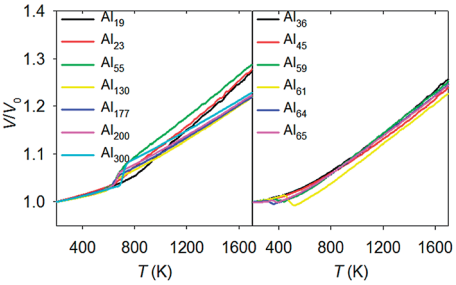

Fig. 18 Volume *vs.* T of aluminum nanoparticles relative to the volume at 200 K. Results are shown for the same nanoparticles as in Fig. 16.

it first decreases and then increases, showing an oscillatory behaviour. On the other hand, for those heat capacity curves without sharp peaks the heat capacity increases slowly and then decreases. The position of the peak does not change much with particle size.

Solid particles should in general be hard to compress and more compact than liquid particles and thus should have smaller volume. As temperature increases, it can be seen that for those particles with a sharp peak in the heat capacity *vs.* T curve, their ln κ increases approximately linearly with temperature at low temperatures, then jumps to higher values, and then it continues to increase nearly linearly with temperature at higher temperatures (Fig. 17). As particle size increases, the ln κ *vs.* T curve also begins to develop a sharp peak. Again the temperature window, in this case for the change from lower ln κ to higher ln κ, becomes narrower for bigger nanoparticles. On the other hand, for the other nanoparticles (except Al_{61}) ln κ increases linearly with temperature until 800–900 K, there is a change in the slope to a gentler slope. For Al_{61} ln κ has a jump between 400 and 500 K, but after the jump ln κ still increases at about the same rate as below 400–500 K until 800–900 K. As Fig. 10 indicates that the population of the GM structure drops to almost zero in this temperature range, a reasonable interpretation is that Al_{61} has a change of structure between 400 and 500 K.

The volumes of the nanoparticles also give valuable information (Fig. 18). For those particles with a sharp peak in heat capacity *vs.* T curve, the volume *vs.* T curve either shows an abrupt change of slope or a jump. For the other particles the volume usually increases gradually with temperature – the

exception being Al_{61}, whose volume has a sudden drop between 400 and 500 K. The coefficient of thermal expansion was studied in the liquid regime from $N = 55$ to $N = 1000$; it increases with increasing particle size and decreases with increasing temperature.[78]

More details can be extracted by analysing various properties during the transition. For example a close examination of the curves for Al_{64} and Al_{65} indicates that their three properties all have a slight change around 400 K, probably indicating a similar structure change as for Al_{61}.

Therefore, the temperature evolution of various properties can provide useful information on the state of nanoparticles. Two common trends can be obtained from these properties: (1) as temperature increases, for some particles the change in the physical properties occurs in an abrupt manner (first-order transition) while for others the change is gradual (second-order transition). (2) The change in the physical properties occurs in a temperature window but not at a definite temperature. The remaining question is: in what state is the nanoparticle below, in, and above the transition temperature window?

With combined information on the physical properties of the nanoparticles, it is clear that below the transition temperature window, the nanoparticles are in the solid state since they have smaller heat capacity, lower compressibility, smaller volume, and smaller size, and these properties are almost a linear function of temperature. Above the transition temperature window, the nanoparticles are in the liquid state since they have higher heat capacity, higher compressibility, larger volume, and larger size. Again, these properties are almost a linear function of temperature. Therefore, we can defines these two regions, a low temperature region and a high temperature where the selected physical properties are almost linear functions of temperature to be the solid state and liquid state of the nanoparticles, respectively. The upper boundary of the low-temperature region is the freezing temperature T_f while the lower boundary of the high-temperature region is the melting temperature T_m. A temperature window between T_f and T_m where the nanoparticles are in the middle of the transition from solid state to liquid state remains to be classified. By further analysing the isomer distribution of the nanoparticles in this temperature window, interesting properties regarding this region can be obtained.

In Fig. 19, the energy distribution of the isomers quenched from the MD simulation of the Al_{70} nanoparticle is shown. It can be seen that at 200 K all the quenched structures are the GM structure. At room temperature, the quenched structures become a mixture of the GM structure and several other low-energy isomers. At 500 K, the populations of high-energy isomers increase, but the populations of the GM structure and low-energy isomers are also non-negligible. At 600 K, the populations of the GM structure and low-energy isomers further decrease, and at 700 K, almost all the quenched structures are high-energy isomers with energies higher than that of the GM structure by 0.9 eV. As temperature further increases, the energy distribution of the quenched structures becomes closer and closer to a Gaussian distribution, and the centre of the

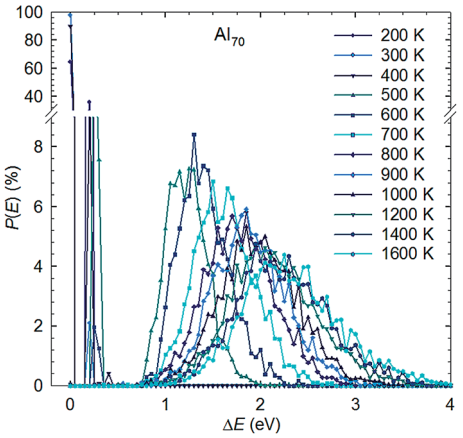

Fig. 19 Percentage ($P(E)$) of quenched structures in the potential energy range between E and $E + \delta E$ with $\delta E = 0.05$ eV for Al_{70}. The abscissa is the potential energy relative to the GM structure. Adapted from ref. 8 with permission from ACS publications.

distribution moves to higher energy. Since the GM structures of nanoparticles often have compact structures[27] and are more rigid than high-energy isomers, they can be viewed as solid-like structures. High-energy isomers, on the other hand can be viewed as liquid like structures. From Fig. 19, we can see there is a transition from the solid-like structures to the liquid-like structures for Al_{70} roughly between 300 and 700 K. In this temperature range, the nanoparticle is a mixture of solid-like structures and liquid-like structures. The energy distribution of the quenched isomers in this temperature becomes bimodal.

The melting points of sodium clusters have been well studied experimentally as function of cluster size.[79] In studying of the melting of sodium clusters, Berry *et al.* found that there is a state in which the solid state and liquid state of the nanoparticle coexist.[80] Our simulation results have provided direct evidence for the coexistence of the two states, showing a bimodal energy distribution of the quenched isomers. We emphasize that the solid-like and liquid-like structures of the nanoparticle are not just two structures but each consists of a set of isomeric structures with similar energy and geometry. For example, for the Al_{56} nanoparticle, its solid state is composed of 56 structures with relative energies within 0.07 eV.[17] Berry named this solid-liquid-coexistence state of nanoparticles the slush state since in this temperature range the nanoparticle is a mixture of solid-like and liquid-like structures and is frequently changing its shape. Thus by analysing the temperature dependence of the various properties of nanoparticles and also the energy distribution of the quenched structures during the MD simulation, we have found and analyzed the three states of nanoparticles, *i.e.*, the solid, slush, and liquid states. The temperature range of the three states for the aluminum nanoparticles are presented in Fig. 20 in a graphic manner where nanoparticles with $T_f = 0$ K do not actually have a T_f of 0 K but are already in the slush state at the starting temperature of the MD simulation (200 K). The plots in Fig. 20 indicate that unlike macroscopic systems, the solid–liquid transition of nanoparticles occurs in a temperature window between T_f and T_m in

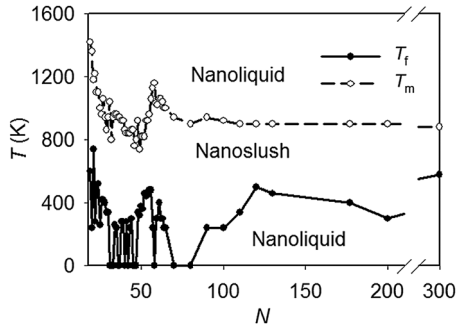

Fig. 20 Freezing temperature (T_f) and melting temperature (T_m) of aluminum nanoparticles.

which the nanoparticles are in a state called the slush state. Fig. 20 shows that the temperature window is not narrow. Many nanoparticles are already in the slush state at room temperature, and the T_f values of most aluminum nanoparticles are below 400 K. Generally the temperature window of the slush state becomes narrower as particle size increases. For the nanoparticles bigger than Al_{100}, T_m does not vary much and is close to the bulk melting temperature of 933 K. We find that T_f is more oscillatory with size than is T_m.

Jarrold, Aguado, and coworkers reported a series of experiments on charged aluminum nanoparticles and computations on charged and neutral aluminum nanoparticles that are very relevant here. Experimental studies[81,82] of positively charged aluminum clusters with $N = 31$–63 revealed a sharp decrease in melting temperature between $N = 55$ and $N = 56$. The experiments also showed that anionic clusters with $N = 51$ and 52 have an extra peak in the heat capacity below the melting temperature. This was interpreted as melting of the surface before the interior melts. They found that the melting temperature is a non-monotonic function of particle size, and that some nanoparticles have prominent peaks in the heat capacity as a function of temperature, whereas others have virtually no peak. The series of studies also included[83] negatively charged aluminum clusters with $N = 35$–70 and concluded, partly on the basis of electronic structure calculations of the GM structures, that both geometric and electronic shell closings (with the latter at $N = 36$, 46, and 66) contribute to the variations in the cohesive energies and latent heats, "but structural changes appear to be mainly responsible for the large variations in the melting temperatures with cluster size." A more recent study[84] included direct dynamics simulations that provided evidence for the slush state. As a result these workers interpreted a first peak in the heat capacity as a transition between a vibrationally excited GM structure and what they called a hot solid phase, and they interpreted the slush regime as a regime of coexistence between the hot solid phase and a phase with diffusive behaviour for all atoms. They also found that electronic shell closings do not persist in the liquid phase. It is encouraging that these finding are basically consistent with our interpretation given above, although they are stated in a different way.

A recent study showed how one can estimate the maximum cluster size for which a range of temperatures can be observed in which solid and liquid coexist.[85] The wider coexistence ranges for metal clusters than for dielectric materials were rationalized in terms of configurational entropy.

Here we provide a few representative references for other computational studies of melting temperature and the temperature and size dependences of the heat capacity for homonuclear metal nanoparticles.[86–92] If one considers nanoalloys, the phase diagram becomes more complicated, and issues of phase separation and ordering have been studied in, for example, Cu–Ag,[93] Pd–Au,[94] Pd–Ag,[95] Pd–Pt,[96] Fe–Au,[97] Rh–Pt,[98] Mg–Al,[99] Ag–Au,[100] and Cs–Na[101] nanoalloys; a review is available.[102]

Melting temperature depression

As we have discussed above, the solid–liquid transition (melting transition) of nanoparticles occurs in a broad temperature window between T_f and T_m. Therefore, strictly speaking, nanoparticles, unlike macroscopic systems, do not have a definite transition temperature (T_t) even if environmental variables such as pressure are fixed. For macroscopic systems, $T_t = T_f = T_m$. For nanoparticles, depending on the physical properties used to characterize the melting one can get different values for T_t that are between T_f and T_m. Therefore there are no unique T_t values for nanoparticles. The peak position (T_p) of the heat capacity *vs.* T curve is one quantity widely used to identify T_t. But we can also define other quantities, for example the peak position of the β (thermal expansion coefficient) *vs.* T curve or the position of the jump of the ln κ (natural logarithm of the compressibility) *vs.* T curve.[8] Since for nanoparticles, as we have discussed above, melting is due to the transformation of the GM structure to other high-energy isomers, we can also define the temperature at which the percentage population of the GM structure among all the quenched isomer structures during the melting simulation drops to 50% (T_{P50}). These definitions give slightly different values for T_t.

Once we have obtained these values the trend in T_t *vs.* size can be obtained. This trend is the nanoparticle analogue of the macroscopic melting-temperature depression. We find that nanoparticles have lower T_t (greater depression) than their corresponding bulk materials, and smaller nanoparticles have even lower T_t. However, that is just a trend; we will see below that the T_t values of some aluminum nanoparticles can even be higher than the bulk value. However, before we discuss these novel properties, we first present the prediction of T_t from thermodynamics considerations.

To extend the thermodynamics for macroscopic systems to nanosystems, Hill introduced a new thermodynamics function X which is the sub-division potential.[9,10] This function characterizes the effect of increasing the number of the systems in the ensemble on the total energy of the ensemble (eqn (7)). By using eqn (5d), the last two terms in eqn (8) can be rearranged from $\mu N_t + X\mathcal{N}$ to $(\mu + X/N)N_t$. The effect of increasing the number of the systems in the ensemble while keeping the total number of atoms in the ensemble fixed is to decreases the system size and to increase the fraction of surface atoms of the nanosystem. Since increasing the fraction of surface atoms increases the

surface chemical potential, we recognize that X/N is the surface chemical potential, to be denoted μ_Σ to distinguish it from the bulk chemical potential μ. Then the classical treatment of the melting of nanoparticles is in line with Hill's formalism of nanothermodynamics.

Based on the above considerations, we relabel the bulk chemical potential as μ_∞, and the molar chemical potential of a nanoparticle can then be expressed as[103]

$$\mu = \mu_\infty + \mu_\Sigma, \tag{29}$$

where

$$\mu_\Sigma = \gamma \frac{\mathrm{d}\Sigma}{\mathrm{d}n}, \tag{30}$$

where Σ is the surface area, n is N/N_A with N_A being Avogadro's number, and γ is the solid–liquid surface tension. For a spherical nanoparticle of radius R, we have surface area Σ equal to $4\pi R^2$ and molar volume V_m equal to $N_A(4/3)\pi R^3$; then

$$\mu_\Sigma = \frac{2\gamma V_m}{R}, \tag{31}$$

and

$$\mu = \mu_\infty + \frac{2\gamma V_m}{R}. \tag{32}$$

Several models for the melting of nanoparticles have been developed.[104] Different models give slightly different temperature dependences of T_t but similar qualitative trends. Here we introduce one of these models. We start by assuming the equilibrium of a solid spherical nanoparticle immersed in its bulk liquid melt. At T_t, the chemical potential of the solid nanoparticle is equal to that of the melt. Since T_t deviates from the bulk melting point ($T_{m,\infty}$), by assuming a first order expansion of μ_∞ with respect to temperature, the following expression for μ_∞ can be obtained at pressure P and temperature T_t:

$$\begin{aligned}\mu_\infty(T_t,\ P) &= \mu_\infty(T_{m,\infty},\ P) + \int_{T_{m,\infty}}^{T_t} \left(\frac{\partial \mu}{\partial T}\right)_P \mathrm{d}T \\ &= \mu_\infty(T_{m,\infty},\ P) - \int_{T_{m,\infty}}^{T_t} S_m \mathrm{d}T,\end{aligned} \tag{33}$$

where $S_m = -\left(\frac{\partial \mu}{\partial T}\right)_P$ is the molar entropy. Then the chemical potential of the solid nanoparticle is

$$\mu_s(T_t,\ P) = \mu_{s,\infty}(T_{m,\infty},\ P) - \int_{T_{m,\infty}}^{T_t} S_{m,s}\mathrm{d}T + \frac{2\gamma V_m}{R}. \tag{34}$$

For the liquid melt, we have

$$\mu_l(T_t,\ P) = \mu_{l,\infty}(T_{m,\infty},\ P) - \int_{T_{m,\infty}}^{T_t} S_{m,l}\mathrm{d}T. \tag{35}$$

At T_t and $T_{m,\infty}$, $\mu_l(T_t, P) = \mu_s(T_t, P)$ and $\mu_{s,\infty}(T_{m,\infty}, P) = \mu_{l,\infty}(T_{m,\infty}, P)$; then it follows that

$$\int_{T_{m,\infty}}^{T_t} (S_{m,l} - S_{m,s})\,\mathrm{d}T + \frac{2\gamma V_m}{R} = 0. \tag{36}$$

Since $S_{m,l} - S_{m,s} \approx \Delta H_{ls}/T$, where ΔH_{ls} is the latent heat of fusion, which does not change significantly with T, we have

$$\begin{aligned}&\Delta H_{ls}\int_{T_{m,\infty}}^{T_t} \frac{1}{T}\mathrm{d}T + \frac{2\gamma V_m}{R} = \Delta H_{ls}\ln\left(\frac{T_t}{T_{m,\infty}}\right) + \frac{2\gamma V_m}{R} = 0, \\ &\ln\left(\frac{T_t}{T_{m,\infty}}\right) = \ln\left(1 + \frac{T_t - T_{m,\infty}}{T_{m,\infty}}\right) = -\frac{2\gamma V_m}{\Delta H_{ls} R}.\end{aligned} \tag{37}$$

Expansion of $\ln\left(1 + \frac{T_t - T_{m,\infty}}{T_{m,\infty}}\right)$ to first order yields

$$\frac{T_t - T_{m,\infty}}{T_{m,\infty}} = -\frac{2\gamma V_m}{\Delta H_{ls} R}. \tag{38}$$

This is the well-known Gibbs–Thomson relation that the melting-temperature depression of nanoparticles is proportional to $1/R$.[105]

For aluminum nanoparticles the T_t values obtained from heat capacity *vs.* T curves are shown in Fig. 21 as a function of N and $1/R$. From Fig. 21 it can be seen that only for particles bigger than Al_{80} is T_t a smooth function of N and $1/R$. Therefore the Gibbs–Thomson relation can only be applied to particles bigger than Al_{80}. For small nanoparticles, T_t shows a strongly oscillatory behaviour. Most aluminum nanoparticles have a lower T_t than bulk aluminum. However, there are a few nanoparticles (Al_{20}, Al_{21}, Al_{22}, Al_{25}, Al_{26}, and Al_{27}) with higher T_t than bulk aluminum. This is a common property of metal nanoparticles and has been observed in experiment for charged aluminum (Fig. 22) and gallium nanoparticles.[49,106] We may also notice that adding or removing one atom from a nanoparticle may cause a jump of more than 100 K in T_t. This has also been confirmed by experimental studies (Fig. 22).[49,106]

Experimental studies involving calorimetric measurement have obtained ΔH_{ls} for metal nanoparticles such as Sn[107] and Al[106,108] nanoparticles. There are different hypotheses for the

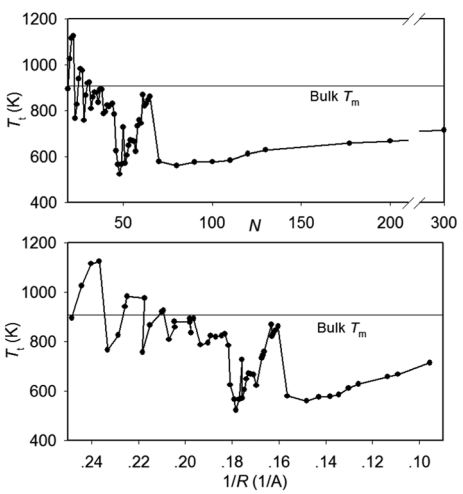

Fig. 21 Melting transition temperature (T_t) of aluminum nanoparticles. Upper: T_t *vs.* N; Lower: T_t *vs.* $1/R$ where R is the radius of gyration at 200 K.

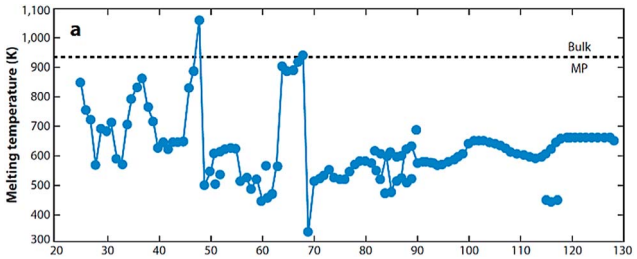

Fig. 22 Melting transition temperature (T_t) of Al_{25}^+–Al_{128}^+ nanoparticles. Reprinted from ref. 106 with permission from Annual Reviews.

size dependence of ΔH_{ls} for nanoparticles. One assumes that it varies with $1/R$ according to[108]

$$\Delta H_{ls}(R) = \Delta H_{ls}(\infty) - \frac{2\gamma V_m}{R}. \quad (39)$$

Another assumes that it is related to $1/R$ by[107]

$$\Delta H_{ls}(R) = \Delta H_{ls}(\infty)\left(1 - \frac{R_0}{R}\right)^3, \quad (40)$$

where R_0 is a fitting parameter with the dimension of length. Experimental results indicate that for larger nanoparticles the size-dependent of ΔH_{ls} fits eqn (40) better than eqn (39).[108] For smaller nanoparticles, the experimental results of Jarrold and co-workers on cationic aluminum nanoparticles indicate that it shows strong oscillatory behaviour.[106] This is an analogue of the strong size dependence of the cohesive energies.[17,106]

Thermodynamic functions

Experimentally it is hard to measure the thermodynamic functions of metal nanoparticles. There are many technical difficulties. For example it is difficult to prepare size-selected nanoparticles with high purity. Except for heat capacity and latent heat of fusion, very little is known experimentally about the thermodynamic functions of metal nanoparticles, except for a few cases such as the heat of formation of Sn nanoparticles.[109] Although electronic structure calculations are able to compute the thermodynamic functions of small molecules with chemical or even sub-chemical accuracy, for metal nanoparticles such calculations are still prohibitively difficult. With the development of an accurate PEF for metal nanoparticles, we are able to provide a systematic way to calculate the thermodynamics functions of metal particles by molecular simulations.

The accurate PEF we use is fitted to data where Al atoms exhibit a wide variety of coordination numbers. Chamaani *et al.*[110] analysed clusters with tetrahedral and truncated octahedral shapes in terms of a model recognizing two kinds of energy contributions, one due to inner atoms and one to surface atoms. This does not seem to recognize the wide variety of coordination numbers in the nanoparticles such that all surface atoms are not equivalent.

Vásquez-Pérez *et al.*[111] used direct dynamics to calculate heat capacities of positively charged nanoparticles of Al with $N = 27$ and 28. Their results show no significant peak for $N = 27$ and a well-defined peak for $N = 28$ at 700 K, whereas experiment[112] shows a broad peak at 700 K for the former case and a sharper peak at 600 K for the latter. By using an analytic PEF, we were able to examine a much larger number of cases, but a disadvantage of using the PEF, as compared to direct dynamics, is that the PEF has been developed only for neutral nanoparticles.

The conventional method to compute molecular thermodynamic functions such as standard-state heat of formation ($\Delta_f H^\circ$) is by computing the atomization energy of the molecule at 0 K. Then from the atomization energy at 0 K and the $\Delta_f H^\circ$ values of the composing atoms at 0 K, the $\Delta_f H^\circ$ of the molecule at 0 K can be obtained by arithmetic. The difference between $\Delta_f H^\circ$ at temperature T (usually room temperature) and $\Delta_f H^\circ$ at 0 K can be obtained from a calculated partition function based on the PEF of the nanoparticle. The partition function is obtained by a sum over states for each structure, with excited vibrational and rotational states making the dominant contribution for most closed shell molecules. If one considers liquids rather than molecules, it is impossible to enumerate all the local minima of the system, and one must use statistical methods to sample the structures. Metal nanoparticles (nanodroplets and nonrigid disordered nanosolids) are between the two extremes of small molecules and bulk liquids, and we will calculate their free energies using a mix of state counting and sampling methods. However, for metal nanoparticles, the accurate calculation of a molecular partition function is not an easy task for the following reasons: (1) the vibrational modes in metal particles are highly anharmonic and nonrigid, with significant vibration-rotation coupling. (2) At room temperature, many metal nanoparticles are already a mixture of many isomer structures. The calculation has to include a large number of isomer structures. (3) As we have discussed above, many metal nanoparticles are already in a slush state at room temperature, and thus the distributions of sizes and shapes of the nanoparticles are strong functions of temperature. Therefore, accurate calculations of partition functions are only possible for very small clusters.

We have computed the partition function of Al_2–Al_4 by Monte-Carlo integration of configuration integrals.[18] The results obtained for Al_2 are close to the most reliable experimental results. However, this method cannot be applied routinely to nanoparticles since it is too expensive. Here we introduce a method to calculate the standard-state free energy of formation of nanoparticles from molecular simulations through the simulation of reaction equilibrium constants.

Consider the reaction

$$A + AN - 1 \leftrightarrow AN, \quad (R1)$$

where A represents a metal atom. The free energy change $\Delta G^\circ(N)$ of reaction R1 under standard state conditions can be obtained from its equilibrium constant. Then the standard-state free energy of formation of A_N is given by a recursion relationship:

$$\Delta_f G^\circ(N) = \Delta G^\circ(N) + \Delta_f G^\circ(N-1) + \Delta_f G^\circ(1), \quad (41)$$

where $\Delta_f G^\circ(1)$ is the free energy of formation of the isolated atom, which is known for most atomic species. We have proposed two methods to compute equilibrium constant of reaction R1 from molecular simulations. The first one is by simulating the formation and dissociation of nanoparticles by aggregation-volume-bias Monte-Carlo (AVBMC) methods.[18,113] The second one is to simulate the forward (formation) and the backward (dissociation) rate constants of R1 by MD simulations.[19] The equilibrium constant can be obtained from the forward and reverse rates by detailed balance. From the simulated equilibrium constant, $\Delta G^\circ(N)$ can be obtained.

The AVBMC and MD simulations are all performed with the analytical NP-B potential, whose evaluation is fast but is less accurate than the NB-A potential and first principle calculations. In addition, the simulations do not include electronic excitations, but their contributions to the standard-state free energy of formation cannot be neglected for metal nanoparticles, especially at high temperatures. Therefore, to obtain accurate $\Delta G^\circ(N)$ for R1 ($\Delta G^\circ_{acc}(N)$) several corrections have to be applied to the simulated $\Delta G^\circ(N)$:

$$\Delta G^\circ_{acc}(N) = \Delta G^\circ(N) + \Delta\Delta E_e^{HLC}(N) + \Delta G_{Elec}(N) + \Delta G_{IsoRov}^{HLC}(N). \quad (42)$$

The first correction in eqn (42) is the high-level correction (HLC) to the potential energy change of R1:

$$\Delta\Delta E_e^{HLC}(N) = \Delta E_e^{HL}(N) - \Delta E_e^{LL}(N), \quad (43)$$

where $\Delta E_e^{HL}(N)$ and $\Delta E_e^{LL}(N)$ are the potential energy change calculated by theoretical methods of the high level (HL) and low level (LL), respectively. In our studies, Kohn–Sham density functional theory with the PBE0 exchange–correlation functional is chosen as HL, while LL is NP-B.

The second correction in eqn (42) is the contribution to $\Delta G^\circ(N)$ of R1 from electronic excitations:

$$\Delta G_{Elec}(N) = -k_B T \ln \frac{q_{Elec}(N)}{q_{Elec}(N-1)q_{Elec}(1)}, \quad (44)$$

The electronic partition functions ($q_{Elec}(N)$) can be computed from electronic excitation energies obtained from time-dependent density functional calculations for small particles. For larger particles this method becomes too expensive, so $q_{Elec}(N)$ is calculated by assuming a distribution of electrons in the Kohn–Sham orbitals by Fermi–Dirac statistics.[18,114] This method requires just a single-point calculation for the electron ground state of the nanoparticle. In principle $q_{Elec}(N)$ should be calculated for every structure, but we assume the electronic partition function is independent of structure, and we calculate it only for the GM structures.

The third correction in eqn (42) accounts for the difference in $\Delta G^\circ(N)$ simulated by a more accurate PEF. Although the simulations are not performed with the more accurate NP-A potential, a correction can be approximately calculated by the following method. Adopting separable assumption of vibrational and rotational motions, the isomeric-vibrational–rotational partition function of a nanoparticle is calculated by

$$q_{IsoRov} = \sum e^{-\frac{\Delta\varepsilon^{(\gamma)}}{k_B T}} q_{Rov}^{(\gamma)}, \quad (45)$$

where $\Delta\varepsilon^{(\gamma)}$ is the energy of isomer γ relative to the GM structure, and $q_{Rov}^{(\gamma)}$ is calculated by the harmonic oscillator-rigid rotator approximation. The correction is then taken as

$$\Delta G_{IsoRov}^{HLC}(N) = -RT \ln \left[\frac{f_{IsoRov}^{HLC}(N)}{f_{IsoRov}^{HLC}(N-1)} \right], \quad (46)$$

with

$$f_{IsoRov}^{HLC}(N) = q_{IsoRov}^{HL}(N)/q_{IsoRov}^{LL}(N), \quad (47)$$

where the HL and LL represent the NP-A and NP-B potentials, respectively.

The $\Delta G^\circ(N)$ values for reaction R1 as obtained by MC and MD simulations are presented as functions of size in Fig. 23. From the figure it can be seen that both MC and MD give quite similar results for $\Delta G^\circ(N)$, and they differ from each other by no more than 4 kcal mol^{-1}. However the two simulations do show a different trend for nanoparticles with size bigger than $N = 30$. For the MC method, $\Delta G^\circ(N)$ gradually increases while for the MD method it always decreases. Similar to the other properties, for larger nanoparticles ($N > 30$ in this case) $\Delta G^\circ(N)$ is almost a smooth function of N. On the other hand, for smaller nanoparticles $\Delta G^\circ(N)$ oscillates with size N.

Adding all the correction terms to $\Delta G^\circ(N)$ simulated by the MC method yields our most accurate estimates, labelled $\Delta G^\circ_{acc}(N)$, shown in Fig. 24. Unlike the uncorrected values, the corrected values show strong oscillatory behaviour as functions of nanoparticle size. This is due to the strong oscillation of $\Delta\Delta E_e^{HLC}(N)$, $\Delta G_{Elec}(N)$, and $\Delta G_{IsoRov}^{HLC}(N)$ with size. All three of these terms are significant. As an example, the electronic excitation contribution to the free energy at 1000 K is −2.8, −0.2, and −1.6 for $N = 37$, 38, 39, respectively, and is −5.8, −0.2, and −1.8 kcal mol^{-1} for $N = 55$, 56, and 67. (Strong size dependence of vibrational contributions was also found in other studies[115,116] of other metal clusters and nanoparticles.) Some corrections reach as high as 30 kcal mol^{-1}. Therefore, thermodynamic values

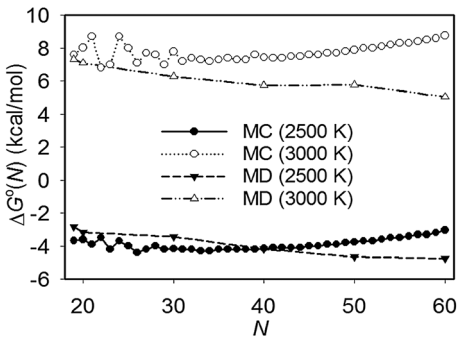

Fig. 23 Simulated values of $\Delta G^\circ(N)$ for reaction R1 as a function of size.

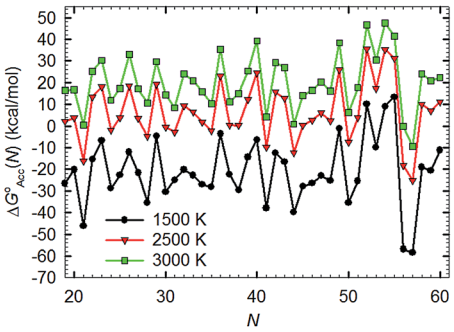

Fig. 24 $\Delta G^{\circ}_{acc}(N)$ of R1 (in kcal mol^{-1}) as a function of size.

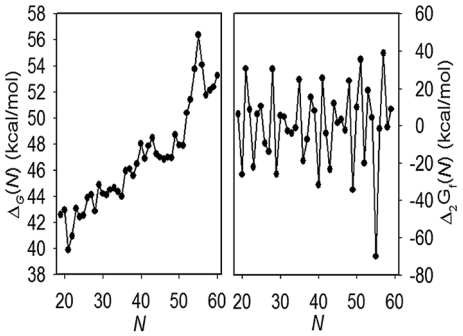

Fig. 25 $\Delta_G(N)$ *vs.* N (left) and $\Delta_2G_f(N)$ *vs.* N (right) at 1500 K.

obtained from molecular simulations using PEFs can only be used as a first step. Due to the difficulty of carrying out accurate calculations, our final free energies are not as reliable as one might wish, but they provide a start on the long-term project of calculating reliable thermodynamics functions for metal nanoparticles.

With $\Delta G^{\circ}_{acc}(N)$ and the reliable experimental free energy of formation for Al atom and Al_2 molecule, $\Delta_f G^{\circ}(N)$ can be obtained for the aluminum nanoparticles as a function of N. With these $\Delta_f G^{\circ}(N)$, quantities similar $\Delta(N)$ and $\Delta_2 E_e^{(1)}(N)$ can be defined to characterize the stability of nanoparticles at temperatures above 0 K. Because $\Delta_f G^{\circ}$ of the bulk metal is zero, a quantity similar to $\Delta(N)$ can be defined as:

$$\Delta_G(N) = \frac{N^{\frac{1}{3}}\Delta_f G^{\circ}(N)}{N} = \frac{\Delta_f G^{\circ}(N)}{N^{\frac{2}{3}}}. \quad (48)$$

Similarly, $\Delta_2 G_f(N)$ can be defined as

$$\Delta_2 G_f(N) = \Delta G_f(N-1) + \Delta G_f(N+1) - 2\Delta G_f(N). \quad (49)$$

The plots for $\Delta_G(N)$ *vs.* N and $\Delta_2 G_f(N)$ *vs.* N are given in Fig. 25. It should be noted that the most stable nanoparticles are those with the most negative $\Delta_G(N)$ or the most positive $\Delta_2 G_f(N)$. It can be seen from the plots that the magic nanoparticles at 0 K become unstable at 1500 K. Al_{55} is an outstanding example for this temperature effect on the stability of nanoparticles. The $\Delta_G(N)$ *vs.* N plot has a very high peak at $N = 55$ while the $\Delta_2 G_f(N)$ *vs.* N plot has a very deep valley at $N = 55$, indicating Al_{55} is very unstable at 1500 K. This conclusion is qualitative in agreement with that obtained by the Gibbs free energy difference as defined by eqn (20) which does not take electronic excitation and other high level corrections into consideration.

Using our free energy changes and the kinetic data for both the forward (formation) and backward (dissociation) reactions for R1, many interesting results can be obtained for the aluminum nanoparticles, for example one can model the homogeneous nucleation of clusters and nanoparticles, which occurs primarily by monomer addition.[117] Significant deviation from the prediction of the classical nucleation theory (CNT) has been found because of the anomalous free energy of the Al_{55} nanoparticle. The calculated steady-state nucleation rates for aluminum nanoparticles are many orders of magnitude lower than those predicted by CNT.

Concluding remarks

Metal nanoparticles are of great importance in technology and have great promise for becoming even more important in future technologies. This article is an overview of recent work on the nanothermodynamics of metal nanoparticles, with most of the examples drawn from our own work on aluminum. Several important conclusions emerge:

Stability of nanoparticles and their multiple structures. Surface effects have a huge impact on the stability of nanoparticles at 0 K. Nanoparticles with extraordinary stability all have well ordered compact geometries with complete geometrical shells. Electronic-shell closings and quantum-size effects play only a minor role in determining the stability of larger nanoparticles, but are significant for smaller nanoparticles. The structural stability of nanoparticles is greatly affected by temperature, and it can only be understood properly, even for a single size of nanoparticle, only by considering multiple structures, often with coordination patterns differing both from small-molecule chemistry and from those found in the bulk. Many nanoparticles already show a population of isomers higher in energy than the global minimum structure at room temperature. Stable structures at 0 K may be unstable at high temperatures. Thus the properties of metal nanoparticles at operando temperatures (often above room temperature) cannot be represented by a single structure, *e.g.* the GM structure. This presents a challenge to theoretical studies on nanoparticles since to obtain reliable results, the properties of many isomeric structures have to be sampled.

The multi-structural aspect of nanoparticles has, it seems to us, been underemphasized. In contrast, there has been a considerable emphasis on the nature of the lowest-energy species for each N. The properties of a metal nanoparticle are an average over its populated structures, and their populations are determined by free energy, not energy. The relative ordering of populations may be quite different from the relative ordering of energies, and in fact the so-called magic number structures (lowest-energy structures of special stability) do not always have the highest populations. Because of experimental difficulties in unravelling the ensemble of dominant structures, computational modelling has irreplaceable value in the field of nanoscience.

Phases and phase changes of nanoparticles. Three phases of nanoparticles have been studied. They are the solid, slush, and liquid phases. The melting transition region of metal

nanoparticles can be either fairly sharp or very broad, depending very sensitively on cluster size, but usually the transition from solid to liquid phases of metal nanoparticles occurs in a wide temperature window in which the nanoparticles are in a slush state. By analysing various properties of the nanoparticles during the transition we have determined the temperature window for the slush state. Many nanoparticles are already in the slush state at room temperature. The transition temperature from solid to liquid phase is usually lower than that of the bulk material, and the degree of depression is found to follow the Gibbs–Thomson relation for aluminum nanoparticles bigger than Al_{80}. However, for smaller particles the transition temperature shows a strong oscillation with size, and for some particles the transition temperature is even higher than that of the bulk material.

Thermodynamic functions of nanoparticles. One often uses the term "classical thermodynamics" to differentiate the traditional study of macroscopic variables from statistical mechanics and statistical thermodynamics, where one relates the macro scale to the atomic scale. Here we have discussed another aspect, namely the differentiation from nanothermodynamics. In this regard we should also emphasize that traditional thermodynamics is based on classical mechanics. The statistical thermodynamics of bulk materials requires a quantum mechanical treatment of atomic-scale phenomena, and the use of quantum mechanics is even more unavoidable for discussing nanoparticles.

The free energy is the single most important thermodynamic property; its knowledge is equivalent to knowing the partition function, from which all thermodynamic variables can be derived. We have proposed a very general method to compute the free energy of formation ($\Delta_f G^\circ(N)$) of metal nanoparticles with a given size (number of atoms N) through molecular simulations based on a potential energy surface obtained from quantum mechanical electronic structure calculations. Molecular simulations using Monte-Carlo or molecular dynamics methods are used to simulate the equilibrium constant of the reaction $A + A_{N-1} \leftrightarrow A_N$. From this equilibrium constant the free energy change of this reaction is obtained; $\Delta_f G^\circ(N)$ can then be obtained by recursion. Various high-level corrections have been applied to $\Delta G^\circ(N)$ to obtain our most accurate estimates of $\Delta_f G^\circ(N)$.

Acknowledgements

The aluminum examples in this article are based on work carried out in collaboration with Ahren Jasper, Nate Schultz, Ilja Siepmann, and Divesh Bhatt, and we thank them for their contributions to this work. This article is based in part upon work supported by the National Science Foundation under Grant no. CHE10-11810.

References

1 R. P. Feynman, *Eng. Sci.*, 1960, **23**, 22–36.
2 R. W. Kelsall, I. W. Hamley and M. Geoghegan, *Nanoscale Science and Technology*, John Wiley, Chichester, England, 2005.
3 M. Hegner and H. J. Guntherodt, *Nanometer Scale Science and Technology – The Impact of STM and AFM*, IOS Press, Amsterdam, 2001.
4 *Metal Nanoparticles: Synthesis, Characterization, and Applications*, ed. D. L. Feldman and C. A. Foss Jr, Marcel Dekker, New York, 2002.
5 J. A. Alonso, *Structure and Properties of Atomic Nanoclusters*, Imperial College Press, London, 2005.
6 *Metal Nanoparticles and Nanoalloys*, ed. R. L. Johnston and J. P. Wilcoxon, Elsevier, Amsterdam, 2012.
7 R. Kubo, *J. Phys. Soc. Jpn.*, 1962, **17**, 975–986.
8 Z. H. Li and D. G. Truhlar, *J. Am. Chem. Soc.*, 2008, **130**, 12698–12711.
9 T. L. Hill, *Thermodynamics of small systems*, W. A. Benjamin, New York, 1963.
10 T. L. Hill, *J. Chem. Phys.*, 1962, **36**, 3182; T. L. Hill, *Nano Lett.*, 2001, **1**, 111–112; T. L. Hill, *Nano Lett.*, 2001, **1**, 159–160; T. L. Hill, *Nano Lett.*, 2001, **1**, 273–275.
11 R. S. Berrry, in *Clusters of Atoms and Molecules*, ed. H. Haberland, Springer-Verlag, Berlin, 1994, pp. 187–204.
12 A. Compagner, *Am. J. Phys.*, 1989, **57**, 106–117.
13 M. Bowker, *Nat. Mater.*, 2002, **1**, 205–206.
14 R. V. Chamberlin, *Nature*, 2000, **408**, 337–339.
15 C. Tsallis, *J. Stat. Phys.*, 1988, **52**, 479–487.
16 C. X. Wang and G. W. Yang, *Mater. Sci. Eng., R*, 2005, **49**, 157–202.
17 Z. H. Li, A. W. Jasper and D. G. Truhlar, *J. Am. Chem. Soc.*, 2007, **129**, 14899–14910.
18 Z. H. Li, D. Bhatt, N. E. Schultz, J. I. Siepmann and D. G. Truhlar, *J. Phys. Chem. C*, 2007, **111**, 16227–16242.
19 Z. H. Li and D. G. Truhlar, *J. Phys. Chem. C*, 2008, **112**, 11109–11121, Erratum, 2009, **113**, 11424.
20 J. C. Tully, *Annu. Rev. Phys. Chem.*, 2000, **51**, 153–178.
21 W. Kohn, *Rev. Mod. Phys.*, 1999, **71**, 1253–1266.
22 J. A. Pople, *Rev. Mod. Phys.*, 1999, **71**, 1267–1274.
23 D. J. Wales, *Mol. Phys.*, 2004, **102**, 891–908.
24 G. Galli and M. Parrinello, in *Computer Simulations in Materials Science*, ed. M. Meyer and V. Pntikis, Kluwer, Dordrecht, 1991, pp. 283–304; J. VandeVondele, M. Krack, F. Mohamed, M. Parrinello, T. Chassaing and J. Hutter, *Comput. Phys. Commun.*, 2006, **167**, 103–128.
25 D. G. Truhlar, in *The Reaction Path in Chemistry: Current Approaches and Perspectives*, ed. D. Heidrich, Kluwer, Dordrecht, 1995, pp. 229–255; J. P. Layfield and D. Troya, *J. Chem. Phys.*, 2010, **132**, 134307.
26 A. D. Becke, *Phys. Rev. A: At., Mol., Opt. Phys.*, 1988, **38**, 3098–3100; J. P. Perdew, *Phys. Rev. B: Condens. Matter Mater. Phys.*, 1986, **33**, 8822–8824.
27 J. P. Perdew, K. Burke and M. Ernzerhof, *Phys. Rev. Lett.*, 1996, **77**, 3865–3868.
28 J. H. Li, X. D. Dai, S. H. Liang, K. P. Tai, Y. Kong and B. X. Liu, *Phys. Rep.*, 2008, **455**, 1–134.
29 A. W. Jasper, P. Staszewski, G. Staszewska, N. E. Schultz and D. G. Truhlar, *J. Phys. Chem. B*, 2004, **108**, 8996–9010.
30 A. W. Jasper, N. E. Schultz and D. G. Truhlar, *J. Phys. Chem. B*, 2005, **109**, 3915–3920.

31 J. P. Perdew, M. Ernzerhof and K. Burke, *J. Chem. Phys.*, 1996, **105**, 9982–9985; M. Ernzerhof and G. E. Scuseria, *J. Chem. Phys.*, 1999, **110**, 5029–5036; C. Adamo and V. Barone, *J. Chem. Phys.*, 1999, **110**, 6158–6170.
32 N. E. Schultz, G. Staszewska, P. Staszewski and D. G. Truhlar, *J. Phys. Chem. B*, 2004, **108**, 4850–4861; N. E. Schultz and D. G. Truhlar, *J. Chem. Theory Comput.*, 2005, **1**, 41–53.
33 D. J. Wales and H. A. Scheraga, *Science*, 1999, **285**, 1368–1372.
34 B. Hartke, *Wiley Interdiscip. Rev.: Comput. Mol. Sci.*, 2011, **1**, 879–887.
35 J. Y. Yi, D. J. Oh and J. Bernholc, *Phys. Rev. Lett.*, 1991, **67**, 1594–1597; R. O. Jones, *J. Chem. Phys.*, 1993, **99**, 1194–1206; L. D. Lloyd, R. L. Johnston, C. Roberts and T. V. Mortimer-Jones, *ChemPhysChem*, 2002, **3**, 408; J. O. Joswig and M. Springborg, *Phys. Rev. B: Condens. Matter Mater. Phys.*, 2003, **68**, 085408; E. J. Noya, J. P. K. Doye and F. Calco, *Phys. Rev. B: Condens. Matter Mater. Phys.*, 2006, **73**, 125407; A. Sebetci and Z. B. Guvenc, *Modell. Simul. Mater. Sci. Eng.*, 2005, **13**, 683–698; A. Aguado, *Comput. Theor. Chem.*, 2013, **12**, 135–143.
36 D. J. Wales and J. P. K. Doye, *J. Phys. Chem. A*, 1997, **101**, 5111–5116.
37 J. Kang, S.-H. Wei and Y.-H. Kim, *J. Am. Chem. Soc.*, 2010, **132**, 18287–18291.
38 X. G. Shao, X. Wu and W. S. Cai, *J. Phys. Chem. A*, 2010, **114**, 29–36.
39 X. G. Shao, X. Wu and W. S. Cai, *J. Phys. Chem. A*, 2010, **114**, 12813–12818.
40 X. Wu and C. D. He, *Chem. Phys.*, 2012, **405**, 100–106.
41 O. Thomas, W. Zheng, S. Xu and K. H. Bowen Jr, *Phys. Rev. Lett.*, 2002, **89**, 213403.
42 P. H. Acioli and J. Jellinek, *Phys. Rev. Lett.*, 2002, **89**, 213402.
43 T. Diederich, T. Döppner, T. Fennel, J. Tiggesbäumker and K. h. Meiwes-Broer, *Phys. Rev. A: At., Mol., Opt. Phys.*, 2005, **72**, 023203.
44 M. Mantina, A. C. Chamberlin, R. Valero, C. J. Cramer and D. G. Truhlar, *J. Phys. Chem. A*, 2009, **113**, 5806.
45 F. Baletto and R. Ferrando, *Rev. Mod. Phys.*, 2005, **77**, 371–423.
46 W. Polak, *Eur. Phys. J. D*, 2013, **67**, 74.
47 T. P. Martin, *Phys. Rep.*, 1996, **273**, 199–241.
48 J. D. Honeycutt and H. C. Andersen, *J. Phys. Chem.*, 1987, **91**, 4950–4963.
49 H. Schnockel, *Chem. Rev.*, 2010, **110**, 4125–4163.
50 M. Brack, *Rev. Mod. Phys.*, 1993, **65**, 677–732.
51 R. Ahlrichs and S. D. Elliott, *Phys. Chem. Chem. Phys.*, 1999, **1**, 13–21.
52 A. Aguado and J. M. Lopez, *J. Chem. Phys.*, 2009, **130**, 064704.
53 O. Kostko, B. Huber, M. Moseler and B. von Issendorff, *Phys. Rev. Lett.*, 2007, **98**, 043401.
54 D. E. Bergeron, P. J. Roach, A. W. Castleman, N. Jones and S. N. Khanna, *Science*, 2005, **307**, 231–235.
55 Z.-G. Zhang, H.-G. Xu, Y. Feng and W. Zheng, *J. Chem. Phys.*, 2010, **132**, 161103.
56 P. Jena, *J. Phys. Chem. Lett.*, 2013, **4**, 1432–1442.
57 A. K. Starace, C. M. Neal, B. Cao, M. F. Jarrold, A. Aguado and J. M. López, *J. Chem. Phys.*, 2008, **129**, 144702.
58 M. Manninen and S. M. Reimann, in *Nanoclusters: A Bridge across Disciplines*, ed. P. Jena and A. Castleman Jr, Elsevier, Amsterdam, 2010, pp. 437–484.
59 M. Yang, K. Jackson and J. Jellinek, *J. Chem. Phys.*, 2006, **125**, 144308.
60 Y. Dong, M. Springborg and I. Warnke, *Theor. Chem. Acc.*, 2011, **130**, 1001.
61 J. Kang and Y.-H. Kim, *ACS Nano*, 2010, **4**, 1092–1098; J. Kang, S.-H. Wei and Y.-H. Kim, *J. Am. Chem. Soc.*, 2010, **132**, 18287–18291.
62 M. F. Jarrold, B. Cao, A. K. Starace, C. M. Neal and O. H. Judd, *J. Chem. Phys.*, 2008, **129**, 014503.
63 Y. Zhai, A. Laio, E. Tosatti and X.-G. Gong, *J. Am. Chem. Soc.*, 2011, **133**, 2535–2540.
64 F. D. Vila, J. J. Rehr, S. D. Kelly and S. R. Bare, *J. Phys. Chem. C*, 2013, **117**, 12446–12457.
65 O. Tishchenko, D. G. Truhlar, A. Ceulemans and M. T. Nguyen, *J. Am. Chem. Soc.*, 2008, **130**, 7000–7010.
66 C. L. Cleveland, W. D. Luedtke and U. Landman, *Phys. Rev. B: Condens. Matter Mater. Phys.*, 1999, **60**, 5065–5077.
67 P. Labastie and R. L. Whetten, *Phys. Rev. Lett.*, 1990, **65**, 1567–1570.
68 D. J. Wales and R. S. Berry, *Phys. Rev. Lett.*, 1994, **73**, 2875–2878.
69 F. Calvo and P. Labastie, *J. Phys. Chem. B*, 1998, **102**, 2051–2059.
70 S. J. Zhao, S. Q. Wang, D. Y. cheng and H. Q. Ye, *J. Phys. Chem. B*, 2001, **105**, 12857–12860.
71 R. S. Berry, in *Strength from Weakness: Strcutural Consequences of Weak Interactions in Molecules, Supermolecules, and Crystals*, ed. A.Domenicano and I. Hargittai, Kluwer, Dordrecht, 2002, pp. 143–168.
72 H. Duan, F. Ding, A. Rosén, A. R. Harutyunyan, S. Curtarolo and K. Bolton, *Chem. Phys.*, 2007, **333**, 57–62.
73 R. S. Berry and B. M. Smirnov, *Phys. Rep.*, 2013, **527**, 205–250.
74 P. W. Atkins, P. W. Atkins and J. De Paula, *Atkins'Physical Chemistry*, Oxford University Press, Oxford, New York, 7th edn, 2002.
75 F. A. Lindemann, *Phys. Z.*, 1910, **11**, 609–615.
76 R. S. Berry and J. L. Krause, *Adv. Chem. Phys.*, 1988, **70**, 35–51; Y. Q. Zhou, M. Karplus, K. D. Ball and R. S. Berry, *J. Chem. Phys.*, 2002, **116**, 2323–2329.
77 P.-H. Tang, T.-M. Wu, P. J. Hsu and S. K. Lai, *J. Chem. Phys.*, 2012, **137**, 244304; P.-H. Tang, T.-M. Wu and S. K. Lai, *J. Phys.: Conf. Ser.*, 2013, **454**, 012026.
78 N. E. Schultz, A. W. Jasper, D. Bhatt, J. I. Siepmann and D. G. Truhlar, Aluminum nanoparticles: Accurate Potential Energy Functions and Physical Properties, in *Multiscale Simulation Methods for Nanomaterials*, ed. R. B. Ross and S. Mohanty, Wiley, Hoboken, 2008, pp. 169–188.

79 W. Schmidt, R. Kusche, B. Von Issendorff and H. Haberland, *Nature*, 1998, **332**, 238–240.
80 R. S. Berry, *Microscale Thermophys. Eng.*, 1997, **1**, 1–18.
81 G. A. Breaux, C. M. Neal, B. Cao and M. F. Jarrold, *Phys. Rev. Lett.*, 2005, **94**, 173401.
82 C. M. Neal, A. K. Starace, M. F. Jarrold, K. Joshi, S. Krishnamurty and D. G. Kanhere, *J. Phys. Chem. C*, 2007, **111**, 17788–17794.
83 A. K. Starace, C. M. Neal, B. Cao, M. F. Jarrold, A. Aguado and J. M. López, *J. Chem. Phys.*, 2009, **131**, 044307.
84 A. Aguado and J. M. López, *J. Phys. Chem. Lett.*, 2013, **4**, 2397–2403.
85 R. S. Berry and B. M. Smirnov, *Entropy*, 2010, **12**, 1303–1324.
86 D. Schebarchov and S. C. Hendy, *J. Chem. Phys.*, 2005, **123**, 104701.
87 R. S. Berry and B. M. Smirnov, *J. Phys. Chem. A*, 2009, **114**, 14220–14226.
88 A. Aguado, *J. Phys. Chem. C*, 2011, **115**, 13180–13186.
89 F. Calvo, E. Pahl, P. Schwerdtfeger and F. Spiegelman, *J. Chem. Theory Comput.*, 2012, **8**, 639–648.
90 S. L. Gafner, J. J. Gafner, I. S. Zamulin and L. V. Redel, *J. Comput. Theor. Nanosci.*, 2012, **9**, 993–1000.
91 Q. Shu, Y. Yang, Y.-T. Zhai, D. Y. Sun, H. J. Xiang and X. G. Gong, *Nanoscale*, 1012, **4**, 6307–6311.
92 A. V. Yakubovich, G. Sushko, S. Schramm and A. V. Solov'Yov, *Phys. Rev. B: Condens. Matter Mater. Phys.*, 2013, **88**, 035438.
93 A. Christensen, P. Stoltze and J. K. Norskov, *J. Phys.: Condens. Matter*, 1995, **7**, 1047–1057.
94 I. Atanasov and M. Hou, *Surf. Sci.*, 2009, **603**, 2639–2651.
95 Y. J. Li, W. H. Qi, B. Y. Huang, M. P. Wang and S. Y. Siong, *J. Phys. Chem. Solids*, 2010, **71**, 810–817.
96 H. Y. Oderji and H. Ding, *Chem. Phys.*, 2011, **388**, 23–30.
97 R. I. González, G. García, R. Ramírez, M. Kiwi, J. A. Valdivia and T. S. Rahman, *Phys. Rev. B: Condens. Matter Mater. Phys.*, 2011, **83**, 155425.
98 J. Pohl, C. Stahl and K. Albe, *Beilstein J. Nanotechnol.*, 2012, **3**, 1–11.
99 Y. Ouyang, P. Wang, P. Xiang, H. Chen and Y. Du, *Comput. Theor. Chem.*, 2012, **984**, 68–75.
100 S. C. Yeo, D. H. Kim, K. Shin and H. M. Lee, *Phys. Chem. Chem. Phys.*, 2012, **14**, 2791–2796.
101 M. H. Ghatee and K. Shekoohi, *Fluid Phase Equilib.*, 2013, **355**, 114–122.
102 Z. Kaszkur, in *Nanoclusters: From Fundamentals to Emergent Applications*, ed. F. Calvo, Elsevier, Amsterdam, 2013, pp. 147–174.
103 E. L. Nagaev, *Phys. Status Solidi B*, 1991, **167**, 381–404.
104 K. K. Nanda, *Pramana*, 2009, **72**, 617–628; Z.-X. Cui, M.-Z. Zhao, W.-P. Lai and Y.-Q. Xue, *J. Phys. Chem. C*, 2011, **115**, 22796–22803; G. K. Goswami and K. K. Nanda, *Curr. Nanosci.*, 2012, **8**, 305–311; R. Overny, Nanothermodynamics and Nanoparticle Synthesis, University of Washington, Seattle, 2010, pp. 16–18.
105 W. Thomson, *Philos. Mag.*, 1871, **4**, 448.
106 A. Aguado and M. F. Jarrold, *Annu. Rev. Phys. Chem.*, 2011, **62**, 151–172.
107 S. L. Lai, J. Y. Guo, V. Petrova, G. Ramanath and L. H. Allen, *Phys. Rev. Lett.*, 1996, **77**, 99–102.
108 J. Sun and S. L. Simon, *Thermochim. Acta*, 2007, **463**, 32–40.
109 T. Bachels, R. Schäfer and H. J. Güntherodt, *Phys. Rev. Lett.*, 2000, **84**, 4890–4893.
110 A. Chamaani, E. Marzbanrad, V. R. Rahimipour, M. S. Yaghmaee, A. Aghaei, R. D. Kamachali and Y. Behnamian, *J. Nanopart. Res.*, 2011, **13**, 6059–6067.
111 J. M. Vásquez-Pérez, P. Calaminici and A. M. Köster, *Comput. Theor. Chem.*, 2013, **1021**, 229–232.
112 C. M. Neal, A. K. Starace and M. F. Jarrold, *Phys. Rev. B: Condens. Matter Mater. Phys.*, 2007, **76**, 054113.
113 B. Chen and J. I. Siepmann, *J. Phys. Chem. B*, 2001, **105**, 11275–11282; B. Chen, J. I. Siepmann and M. L. Klein, *J. Phys. Chem. B*, 2001, **105**, 9840–9848; B. Chen, J. I. Siepmann, K. J. Oh and M. L. Klein, *J. Chem. Phys.*, 2001, **115**, 10903–10913.
114 P. Srepusharawoot and U. Pinsook, *Phys. Status Solidi B*, 2005, **242**, 1598–1605.
115 V. G. Grigoryan and M. Springborg, *Phys. Rev. B: Condens. Matter Mater. Phys.*, 2011, **83**, 155413.
116 Y. Dong, M. Springborg and I. Warnke, *Theor. Chem. Acc.*, 2011, **130**, 1001–1008.
117 S. L. Girshick, P. Agarwal, B. M. smirnov and D. G. Truhlar, *J. Chem. Phys.*, 2009, **131**, 134305.

